TOPICAL REVIEW • OPEN ACCESS

Neutron studies of Na-ion battery materials

To cite this article: Ami R Shah *et al* 2021 *J. Phys. Mater.* **4** 042008

View the article online for updates and enhancements.

Journal of Physics: Materials

TOPICAL REVIEW

Neutron studies of Na-ion battery materials

Ami R Shah[1] , Rebecca R C Shutt[2] , Keenan Smith[1], Jennifer Hack[1] , Tobias P Neville[1],
Thomas F Headen[3], Dan J L Brett[1,4], Christopher A Howard[2], Thomas S Miller[1,4] and Patrick L Cullen[5,*]

[1] Electrochemical Innovation Laboratory, Department of Chemical Engineering, University College London, Gower Street, London
WC1E 6BT, United Kingdom
[2] Department of Physics and Astronomy, University College London, Gower Street, London WC1E 6BT, United Kingdom
[3] ISIS Neutron and Muon Source, Rutherford Appleton Lab, Harwell Campus, Oxford OX11 0QX, United Kingdom
[4] The Faraday Institution, Quad One, Becquerel Avenue, Harwell Campus, Oxford OX11 0RA, United Kingdom
[5] School of Engineering and Materials Science (SEMS) and Material Research Institute, Queen Mary University of London, Mile End
Rd, Bethnal Green, London E1 4NS, United Kingdom
[*] Author to whom any correspondence should be addressed.

E-mail: p.cullen@qmul.ac.uk

Abstract

The relative vast abundance and more equitable global distribution of terrestrial sodium makes sodium-ion batteries (NIBs) potentially cheaper and more sustainable alternatives to commercial lithium-ion batteries (LIBs). However, the practical capacities and cycle lives of NIBs at present do not match those of LIBs and have therefore hindered their progress to commercialisation. The present drawback of NIB technology stems largely from the electrode materials and their associated Na^+ ion storage mechanisms. Increased understanding of the electrochemical storage mechanisms and kinetics is therefore vital for the development of current and novel materials to realise the commercial NIB. In contrast to x-ray techniques, the non-dependency of neutron scattering on the atomic number of elements (Z) can substantially increase the scattering contrast of small elements such as sodium and carbon, making neutron techniques powerful for the investigation of NIB electrode materials. Moreover, neutrons are far more penetrating which enables more complex sample environments including *in situ* and *operando* studies. Here, we introduce the theory of, and review the use of, neutron diffraction and quasi-elastic neutron scattering, to investigate the structural and dynamic properties of electrode and electrolyte materials for NIBs. To improve our understanding of the actual sodium storage mechanisms and identify intermediate stages during charge/discharge, *ex situ, in situ*, and *operando* neutron experiments are required. However, to date there are few studies where *operando* experiments are conducted during electrochemical cycling. This highlights an opportunity for research to elucidate the operating mechanisms within NIB materials that are under much debate at present.

1. Introduction

The ever increasing number of applications for energy storage devices has made their existence vital in everyday life. Rechargeable batteries have played essential roles for energy storage due to their high energy densities [1]. However, improvements to existing technologies are still necessary to make rechargeable batteries the least expensive and most environmentally benign of the current energy storage devices.

Since commercialisation in 1991 [2], rechargeable lithium-ion batteries (LIBs) have been used in a wide range of applications from small, portable electronic devices to electric vehicles (EVs) and hybrid electric vehicles (HEVs). To meet the rising consumer demands of EVs and HEVs, rechargeable batteries for these purposes are now required to complete faster charges, sustain longer cycle lives, and exhibit higher capacities. Addressing these demands requires investigating alternative electrode materials and utilising suitable characterisation techniques to explore the mechanisms within rechargeable battery materials.

Typically, the charge carrier for most rechargeable batteries in EVs and HEVs is lithium due to its outstanding electrochemical properties, small size, and low mass. Lithium is one of the lightest (6.94 g mol^{-1}) and most electropositive (-3.05 V vs standard hydrogen electrode) of the elements [3]. These properties allow the efficient uptake of Li$^+$ ions between the different electrodes, giving LIBs their fast charging qualities. Despite these advantageous qualities, lithium also has considerable disadvantages. Irregular deposition of metallic lithium often occurs upon continuous and extensive cycling, and can cause dendrite formation [4]. Dendrites can lead to short circuits, cell failure, thermal runaway, and fires [5]. Another major drawback to lithium is its limited terrestrial abundance which will inevitably lead to its higher cost, potentially making lithium less feasible in the future. A recent study predicted that considering the known economically viable lithium reserves, the available lithium could be exhausted by the mid-21st century [6]. For these reasons, attention has turned to a similar, yet more abundant and cheaper, element, sodium.

1.1. Sodium-ion batteries (NIBs)

Conventional NIBs operate with the same working principles of LIBs, yet their fully commercial adoption is hindered predominantly due to the processes at and within the electrode materials. The most common anode material for LIBs is graphite, which consists of stacked sheets of carbon atoms arranged in a hexagonal structure. Strong covalent bonding of sp^2 carbon atoms holds the structure together in the intraplanar direction, while weaker van der Waals forces hold the sheets together in the interplanar direction. Graphite's semimetallic nature enables the efficient incorporation of guest ions between the sheets by a process known as intercalation. The resulting intercalation products are classed as graphite intercalation compounds (GICs) and it is well known that graphite forms thermodynamically stable GICs, for example with lithium (LiC$_6$) and potassium (KC$_8$) in their most metal-concentrated stoichiometries [7].
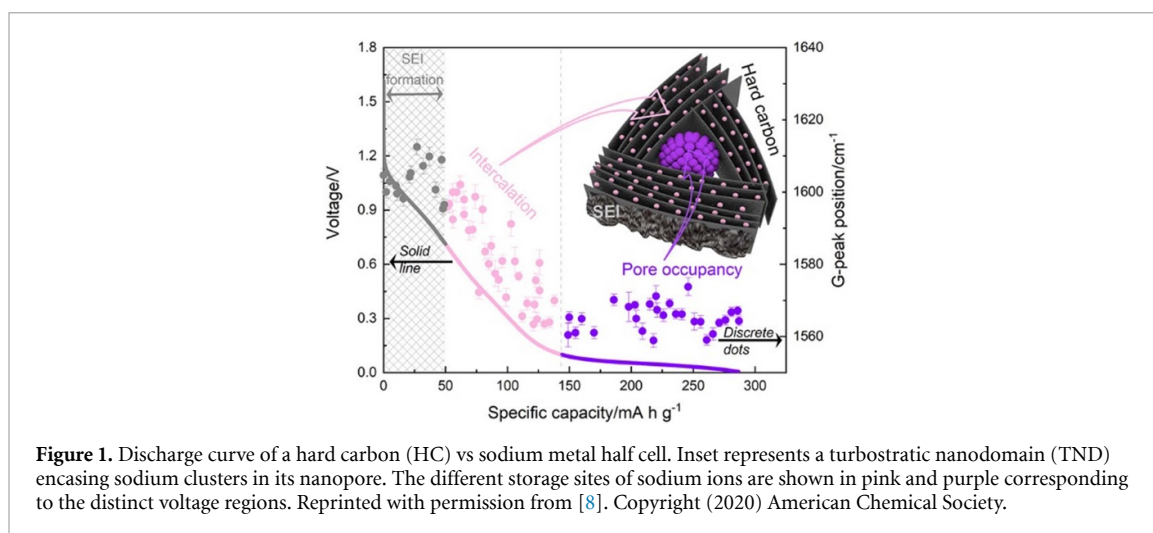
Due to the energetics being unfavourable, sodium only dopes into graphite under non-ambient conditions. With the exception of lithium, the formation energies of group 1 metal GICs decrease moving down the group, hence the GICs become more stable [9, 10]. The lack of stable, high stoichiometry Na GICs has meant that graphite is incompatible as an anode material in NIBs, therefore alternative materials are necessary for this technology. In recent years, attention has been drawn to disordered carbonaceous materials such as hard carbon (HC) [11, 12], which in fact was one of the first anode materials employed by Sony during commercialisation of LIBs [13]. HCs comprise of non-graphitisable carbons arranged in randomly oriented turbostratic nanodomains (TNDs) [14]. The turbostratic arrangement and curved nature of the TNDs allows for a larger interlayer spacing than graphite and the material contains appreciable nanoporosity with pore-size similar to the size of graphene sheets in the nanodomains. HCs can accommodate Na$^+$ ions in three different ways:

- Among the interlayer spaces enclosed by the TNDs.
- Within the empty nanopore/micropore voids.
- Upon edge/defect sites on the pore surfaces through vacancies, dangling bonds and functional groups.

As a result of the various storage mechanisms of HC and the nature of the storage sites, two characteristic regions are observed in the voltage vs capacity curve of Na-ion half cells (figure 1). Although there has been much debate over the true origins of these regions, the general consensus at present is that the 'sloping' region ($\sim$1.0–0.1 V vs Na) corresponds to Na$^+$ ions intercalating into the interlayer sites and storage at low energy binding sites such as at defects and pore surfaces. The 'plateau' region ($\sim$0.1–0.0 V vs Na) arises from the formation of metallic Na clusters within nanopores [8, 12, 15–18]. Both regions are illustrated in figure 1. In contrast, some studies have proposed that intercalation is associated with the plateau region [19, 20], however, this theory has been disputed by others [8, 15, 17].

Although HC electrodes are promising for NIB technology with the various storage sites within their structures, to date the highest reversible capacity achieved is $\sim$300 mA h g^{-1} [19, 21]. To compete against LIB anodes with practical reversible capacities of $\sim$400 mA h g^{-1}, tuning of HC structures for NIB electrodes is required to increase the capacity. To this end, advanced characterisation techniques such as *operando* neutron diffraction are imperative to indicate which tuneable properties of the HC structures are of importance when considering the cycling of NIBs.

Cathode materials for NIBs can be similar to those of LIBs. For example, layered sodium oxides have shown the most promising electrochemical performances. These materials are known to exist in different phases depending on Na content and therefore undergo phase transitions during charging and discharging. Phase changes often hinder cycling ability by causing strain on the electrode structures, leading to electrode

Figure 1. Discharge curve of a hard carbon (HC) vs sodium metal half cell. Inset represents a turbostratic nanodomain (TND) encasing sodium clusters in its nanopore. The different storage sites of sodium ions are shown in pink and purple corresponding to the distinct voltage regions. Reprinted with permission from [8]. Copyright (2020) American Chemical Society.

cracking [22–24]. Identifying specific phases at certain states of charge through *ex situ* neutron studies can be useful for determining which phases are most stable with a high amount of sodium and therefore are able to retain more capacity.

The all-solid-state NIB is another emerging topic of interest in energy storage research. Its general working principles are similar to those of commercial LIBs, however, all-solid-state batteries are much safer. To eliminate the dangers associated with highly flammable liquid electrolytes in conventional LIBs and NIBs, all-solid-state batteries utilise non-flammable solid-state electrolytes (SSEs). SSEs also allow the use of high energy density metal anodes that pose safety concerns related to dendrites in conventional LIBs. Some intrinsic requirements of an electrolyte include a stable electrochemical window, minimal volume expansion, and high ionic conductivity. High ionic conductivity is often difficult to achieve with solid-state materials therefore careful consideration is necessary when synthesising potential SSE materials. Additionally, large volume changes can lead to electrode/solid electrolyte delamination which disconnect Na^+ ion pathways. Quasi-elastic neutron scattering (QENS) is a useful technique for analysing Na^+ ion movement within SSEs and therefore provides valuable insights into the nature of the Na^+ ion shuttling mechanisms under battery operating conditions.

Electrode materials for NIB technology must also possess various fundamental properties to function well in a battery. Some of these properties include high electronic conductivity, energy density, and structural stability. Other factors that do not concern their performance but are of equal importance are material cost, abundance, and sustainability. The former properties can be directly derived from electrochemical and material characterisation studies. Improvements on the latter properties can be made by synthesising alternative materials with the aid of results from the characterisation studies. To this end, characterisation techniques such as neutron scattering with complementary electrochemical analysis are required to combat the current limitations within NIB technology.

1.2. On the use of neutrons for studying NIB materials

Neutrons have no charge, their electric dipole moment is either zero or too small to be measured, and they are far more penetrating than charged particles. These intrinsic properties allow for neutrons to travel large distances without being scattered or absorbed, unlike x-rays. Neutrons are also far less destructive to the material under analysis than x-rays. The energy of an x-ray photon with a wavelength of 1.5 Å is over 10^5 times greater than that of the energy of a neutron of the same wavelength [25]. However, neutron beams have low intensities therefore neutron scattering is often a signal-limited technique that requires careful data reduction, refinement, and fitting procedures [26]. Nevertheless, neutron characterisation techniques are extremely powerful for providing insights into material structures, and can provide complementary information to x-ray studies of materials.

For the study of LIB and NIB electrode materials, there is significant research that employs XRD. X-rays are relatively cheaper to generate than neutrons and so most research laboratories can purchase XRD instruments, making this technique efficient and convenient for analysing crystal structures. Unlike the ease of x-ray generation, generating neutrons with high flux requires nuclear fission reactors or accelerator-based pulsed sources, hence neutron studies are confined to only 23 dedicated research facilities around the world

[27]. X-ray scattering amplitude is dependent on the number of electrons, and therefore excels at detecting atoms of elements with higher atomic numbers. The scattering amplitude of neutrons, on the other hand, has no dependence on the atomic number of the element since neutrons interact with matter via nuclear forces. For these reasons, neutron diffraction can also be used to distinguish between light atoms, isotopes, and elements of similar atomic number, making it an effective technique for the study of the movement of Li^+ and Na^+ ions within electrode materials [26].

The dynamics of ions is critical to understand electrochemical mechanisms in both electrodes and electrolytes. QENS can provide temporal and spatial understanding to diffusion type, such as the distance and rate of ion jumps, at the atomic scale and ns–ps timescales. By coupling QENS observation with structural understanding of the materials, macroscale conductivities and molecular dynamics (MD) simulations, a complete picture of the electrochemical mechanisms may be obtained. Information regarding the movement of species within these critical materials and the effect of various factors may then be extracted, with the ultimate aim to guide future material design, synthesis, and treatment.

In LIB research, various neutron techniques have been employed for *in situ* and *operando* studies [28–32], however, to date, the same is not true for NIB research. To our knowledge, NIB advanced characterisation reviews such as [33, 34] only include short sections on neutron studies and the recent review by Shen *et al* [35] only concerns layered oxide cathode materials. There is little research on *ex situ* studies where the electrode materials have been analysed pre- and post-use in battery conditions. Furthermore, there is scarce research on *in situ* or *operando* neutron characterisation techniques where neutrons are fired at the electrode materials whilst they are being charged or discharged under battery conditions. While there is a myriad of neutron techniques employed in LIB research (e.g. reflectometry, radiography and small angle scattering), this article focuses on neutron diffraction and QENS studies for NIBs. We review neutron studies of as-made NIB cathode and anode materials (prior to being processed as electrodes) and electrolytes developed to date, and highlight the lack of research on neutron studies during and after battery operation.

2. Neutron techniques

2.1. Introduction to neutron scattering and definitions

This section provides a basic introduction to neutron scattering and the material information that can be extracted from these techniques. For a deeper understanding of this method, we recommend [36].

In any neutron experiment, an incident beam of neutrons is directed at a sample, known as the scattering system, as shown in figure 2. By counting the number of neutrons scattered into the solid angle, $d\Omega$, per second, the differential cross section, $\frac{d\sigma}{d\Omega}$, can be defined as shown in equation (1). The term, I_0, refers to the neutron flux which is the number of incident neutrons through the unit area per second:

$$\frac{d\sigma}{d\Omega} = \frac{\text{No. of neutrons scattered per second into a solid angle}}{I_0 d\Omega}. \tag{1}$$

Considering a single fixed nucleus, its interaction with neutrons will be elastic, where the energy of the scattered neutrons remains the same and the magnitude of the incident wavevector, $\boldsymbol{k}$, will be equal to the scattered wavevector, $\boldsymbol{k'}$, according to figure 3. This allows the differential cross section to equal the square of the scattering length of the nucleus, b, as shown in equation (2):

$$\frac{d\sigma}{d\Omega} = b^2. \tag{2}$$

Then, adding up the neutrons scattered by many nuclei with the same scattering lengths in the system gives:

$$\frac{d\sigma}{d\Omega} = \sum_{i,j} b_i b_j e^{-i\boldsymbol{Q}(\boldsymbol{R}_i - \boldsymbol{R}_j)} \tag{3}$$

where $\boldsymbol{R}_i$ is the position vector for nucleus i and $\boldsymbol{Q}$ is the scattering wavevector (figure 3).

In reality, the scattering lengths of all the nuclei (even of the same element) within a scattering system are not equal. Scattering lengths depend on the particular nucleus and the spin state of the nucleus-neutron system. Assuming there is no correlation between the scattering lengths of different nuclei, the differential cross section now becomes:

$$\frac{d\sigma}{d\Omega} = \langle b \rangle^2 \sum_{i,j} e^{-i\boldsymbol{Q}(\boldsymbol{R}_i - \boldsymbol{R}_j)} + N\left(\langle b^2 \rangle - \langle b \rangle^2\right) \tag{4}$$
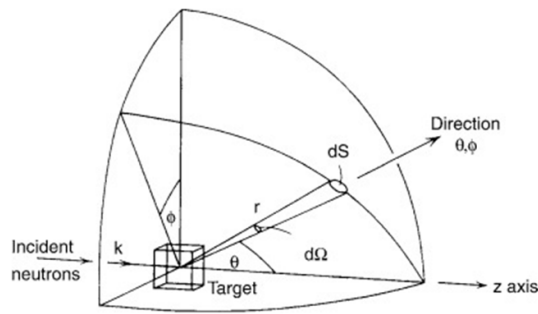
Figure 2. Diagram showing the geometry for a neutron scattering experiment. Reproduced with permission from [36]. [Cambridge University Press].
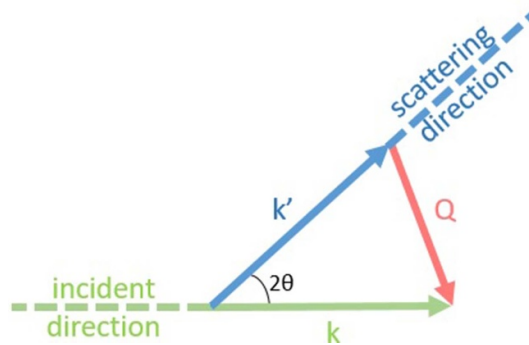
Figure 3. A scattering triangle of an elastic scattering event where the scattering vector, *Q*, is related to the incident wavevector, *k*, and the scattered wavevector, *k'*.

where N is the total number of atoms in the scattering system. Equation (4) is made up of two terms; coherent scattering and incoherent scattering. Coherent scattering depends on the correlation between same and different nuclei, therefore it gives interference effects and can give information about structure. Incoherent scattering depends on correlations between the positions of the same nucleus at different times.

In a total neutron scattering experiment, the differential cross section is measured and plotted against *Q*. Peaks in this plot arise from the correlated lengths within the sample, d, which can be calculated using equation (5):

$$Q = \frac{2\pi}{d}. \tag{5}$$

Peak intensities are associated with the scattering length densities of the atoms within the sample. Small angle neutron scattering (SANS) measures scattering at low *Q*, and therefore probes longer range structures in materials, up to tens of nanometres. The technique probes the interface between bodies with different scattering making it particularly useful for materials like HCs containing pores. Unlike crystalline compounds, HCs do not exhibit well-defined crystal planes and therefore do not give well-defined peaks in their diffraction patterns. However, useful information from SANS can be extracted from the low *Q* region that concerns correlated lengths in the nanometre scale. These are on the order of pore sizes within HCs and therefore can give insights regarding the pore size and changes in composition.

2.2. Neutron diffraction
Neutron diffraction is the simplest type of coherent neutron scattering. Scattered waves can interfere with each other. Constructive interference occurs when the scattered waves reinforce each other, as a result of them being in-phase (whereas waves that are out-of-phase cancel each other out and cause destructive interference). The conditions for constructive interference are captured by Bragg's law, illustrated in figure 4 where d is the distance between adjacent planes, and θ is the angle between the incident beam and the plane of atoms. The scattered waves from adjacent planes must travel a path difference equal to $2d\sin\theta$ to remain in-phase. This occurs when the path difference is equal to an integer, n, of the wavelength of radiation, λ, as shown in equation (6):

$$n\lambda = 2d\sin\theta. \tag{6}$$
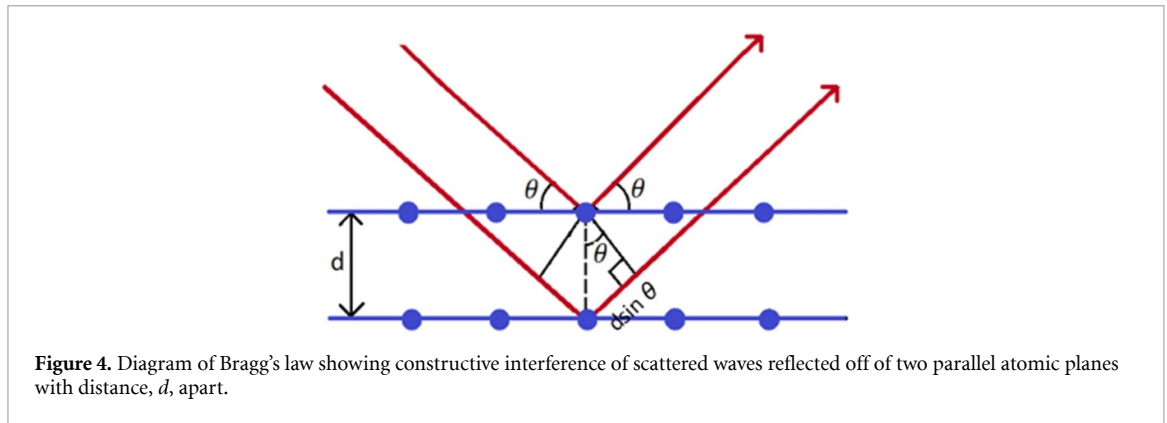
Figure 4. Diagram of Bragg's law showing constructive interference of scattered waves reflected off of two parallel atomic planes with distance, *d*, apart.

Bragg peak angles are associated with well-defined atomic planes and the *d*-spacings of the different planes of the lattice of interest. This information, and their relative intensities can be used to deduce symmetry, phases and distances between atoms.

For single crystals, the sample must be correctly oriented to the incident neutron beam to obtain Bragg diffraction peaks for specific planes of atoms. Typically, any orientation of a polycrystalline powder sample will give Bragg diffraction peaks for all *d*-spacings within the crystal as there will always be grains in the correct orientation. This method is neutron powder diffraction (NPD) and is commonly used for battery electrode materials which consist of many randomly oriented single-crystal grains [26, 37].

Since neutron diffraction is a type of coherent neutron scattering, it concerns the first term of equation (4) and requires incoherent scattering to be removed from the measurement. It measures the structure factor, $S(\boldsymbol{Q})$, (given in equation (7)), which contains information about the correlations between atoms:

$$S(Q) = 1 + \int g(R) \cdot e^{-iQR} dR \tag{7}$$

$$g(R) = \sum_{i \neq 0} \langle \delta(R - R_i + R_0 \rangle. \tag{8}$$

The structure factor contains the term $g(R)$ which is known as the static pair correlation function, given in equation (8). It determines the probability of finding an atom *i* at a distance *R* from another atom at the origin of the system.

Once neutron diffraction data is retrieved, there are different methods that can be used to extract specific information about the sample. For example, Rietveld refinement is mostly used to refine lattice parameters, atomic parameters, and atomic site occupancies. It employs a method of least squares to fit a calculated diffraction pattern (from Fourier transforms) to the experimentally obtained diffraction pattern. The neutron pair distribution function (nPDF) method requires a wide range in $\boldsymbol{Q}$-space to be measured in order to obtain an accurate Fourier transform to real space. This is optimally achieved by specific instruments at pulsed neutron sources where a wide range of neutron wavelengths (thermal and epithermal), coupled with a wide solid angle coverage afford a wide simultaneous $\boldsymbol{Q}$ range. The resulting total pair distribution function, $G(r)$, gives a view of the local structure with materials allowing structural analysis of liquid, amorphous, semi-crystalline, and highly defective systems. Both Rietveld refinement and nPDF analyses can identify distinct phases of NIB electrode materials and exactly where Na^+ ions reside, therefore they can provide information about Na storage and how the structures may be improved to increase the Na^+ ion occupancy. This understanding could lead to an increase in the material's specific capacity, enhancing its electrochemical performance.

2.3. Quasi-elastic neutron scattering (QENS)

QENS investigates dynamical relaxation processes in a system, observed by broadening of the elastic scattering signal as an energy transfer ($E = \hbar \omega$) function. Observable dynamics occur within the timescale of the spectrometer set by the instrumental resolution function; the minimum measurable energy exchange. At low resolution, high energy neutrons probe fast motions with correspondingly large energy exchange, while at high resolution, low energy neutrons probe slow motions with correspondingly small energy exchange. 'Immobile' species (moving slower than the instrument resolution) are contained within the elastic scattering signal, $\delta(\omega)$, while dynamics faster than the window give rise to an extremely broad signal that is modelled by an approximately flat background function, $B(\boldsymbol{Q})$. Analysis is carried out as a function of

multiple scattering vectors and the scattering function, $S(Q, \omega)$, contains information about the spatial (Q) and temporal (ω) correlation between identical nuclei (S_{inc}) and the static and dynamic correlations of distinct nuclei (S_{coh}) [38]. Considering the incoherent scattering term, the measured QENS signal can be deconvoluted into vibrational, rotational, and translational components:

$$S_{inc}(Q, \omega) = S_{vib}(Q, \omega) \otimes S_{rot}(Q, \omega) \otimes S_{trans}(Q, \omega) \otimes R \qquad (9)$$

where R is the experimentally determined instrumental resolution function, obtained from a vanadium standard convoluted with a $\delta(\omega)$ Dirac delta function. To a very good approximation, the QENS broadening due to rotational and translational components, in equation (9), can be modelled using one or more Lorentzian functions fitted to the experimental data, each correlated to a unique dynamical contribution in the sample. The resulting Lorentzian fits are analysed by examining the correlation of the relaxation time (τ) for the process involved, obtained from the inverse of the half width at half maximum (HWHM, Γ). Depending on the degree of localisation of the dynamics probed for different types of motion and excitations, the τ vs Q^2 relation shows non-dispersive (localised ion-hopping or reorientation/rotations) or dispersive (i.e. centre-of-mass displacements of the scattering unit) motions. Diffusional motions result in a dispersive $\Gamma(Q^2)$ relation which is analysed according to one of a number of possible jump-diffusion models, including;

- Chudley–Elliot (CE) model [39]—particles reside at a given site, vibrating about a centre of equilibrium, and then undergo instantaneous jumps between sites defining a regular lattice.
- Singwi–Sjölander (SS) model [40]—particles continuously alternate between oscillating for a mean time and undergoing directed continuous motion (diffusion) for a mean time.
- Hall–Ross (HR) model [41]—particles undergo a random-walk diffusion with a Gaussian distribution of jump lengths within a restricted volume.

At low Q, dynamics follow Fick's law where diffusion occurs via infinitely small, elementary jumps, allowing the self-diffusion coefficient, D, to be deduced from the HWHM, regardless of the model used. Deviation from Fick's law due to stronger interactions at high Q allow identification of specific parameters occurring within the jump mechanism such as average diffusion length and residence times.

Fixed window scans reveal changes in dynamical behaviour as a function of Q or temperature for a given instrument's accessible timescale. During a fixed window scan, the elastic intensity (EFWS) or the intensity at a fixed inelastic energy transfer (IFWS) is measured as a function of temperature. Dynamical signatures appear as changes in slope on the EFWS or slope changes and maxima in the IFWS. Assuming harmonic and isotropic vibrational oscillations, information of the temperature dependence of the mean squared displacement, $\langle u^2 \rangle$, of mobile particles can be obtained from the EFWS intensity using equation (10):

$$I_{elastic}(Q, T) = \exp\left[-\frac{Q^2 \langle u^2(t) \rangle}{3}\right]. \qquad (10)$$

$S_{inc}(Q, \omega)$ contains not only information about the relaxation dynamics of species (quasi-elastic component), but also their relative spatial arrangement (elastic component) within the instrumental time resolution, to provide geometry of rotational or confined translational movements. The elastic incoherent structure factor (EISF) is the fraction of elastic contribution to the signal, determined by fitting the total intensity with a model accounting for both the elastic and quasi-elastic contributions, and is calculated according to equation (11):

$$\text{EISF}(Q) = \frac{I_{inc}^{el}(Q)}{I_{inc}^{el}(Q) + I_{inc}^{qe}(Q)} \qquad (11)$$

here, $I_{inc}^{el}(Q)$ and $I_{inc}^{qe}(Q)$ are the elastic and quasi-elastic intensities, respectively. Elastic incoherent scattering occurs when the motion is confined in space, as Q increases and thus a smaller volume is probed, the EISF decays to zero as the process appears more diffusive. The comparison of the experimental EISF vs Q with a theoretical EISF vs Q derived from a model makes it possible to access the geometry of a particle motion. This analysis allows determination of the proportion of mobile particles on the time scale of the instruments along with the proportion of particles involved in local jumps and long range diffusion.

QENS is predominantly performed on systems where hydrogen dynamics are of interest, due to its vastly greater incoherent to coherent scattering cross section (80.27 vs 1.76 barn, respectively) and dominating effect compared to other elements. Whilst much lower than H, Na has a reasonably large incoherent scattering cross section, compared to many elements in NIB materials (e.g. Al, O, P, and C) but has an equally

large coherent cross section (1.62 vs 1.66 barns, respectively). Therefore, successful investigation needs well designed experiments, with a long duration required to obtain representative statistics, particularly in the absence of H (complete water removal) which is common in most battery materials. Data analysis must also consider contributions from coherent scattering, S_{coh}^{NaNa}. The poor statistics from Na scattering, means that other techniques such as density functional theory (DFT), MD, and pulsed-field gradient nuclear magnetic resonance (NMR) spectroscopy, greatly compensate observations during dynamic events.

For an in-depth understanding of QENS theory, technique, and applications, we recommend further reading such as [38, 42].

2.4. Instrumentational background

Neutrons can be generated by nuclear fission in a reactor or by spallation. Reactors produce a continuous neutron beam of 0.1–10 MeV by splitting isotopes of heavy atoms (usually uranium or plutonium) into smaller atoms. Spallation produces pulses of neutrons of about 1 GeV and involves a heavy metal target (usually tungsten), which is bombarded by high-energy protons. In both cases, neutrons are then thermalized by a moderator (usually hydrogen or water) to the thermal region with energies of 5–100 meV before interacting with the sample [25]. Once thermalized, neutrons are collimated into a narrow beam, typically a few cm in size, through holes in shielding blocks, and directed towards the scattering system. With the pulsed beam from spallation sources, the neutrons from each pulse are produced at the same time and so their time of flight (TOF) to the detector can be used to measure their energies. Most neutron detectors use ^{3}He which absorbs the scattered neutrons and undergoes ionisation to ^{3}H and a proton, both of which are collected at an electrode [26]. There are many types of neutron instruments that are too various to cover in this review.

Most sources in current operation have maximum neutron flux of about 10^{15} neutrons cm^{-2} s^{-1} at the beam tubes, and the neutron flux will be lower than this value at the different instruments [25]. The absorption cross section of an atom is defined as the probability per unit time that a neutron incident on that atom is absorbed by the nucleus. This gives rise to radioactivity in the samples after measurements, requiring them to be left under quarantine for a period of time before they are safe to handle again. Samples containing a high proportion of atoms with high absorption cross sections will reduce the amount of signal detected from scattering events. The absorption cross section of Na in its natural isotopic abundance is 0.53 barns, compared to 70.5 barns for Li, making Na-ion cells better suited to be probed with neutrons with the metals in their natural abundance when compared to analogous Li-ion cells. For this reason, lithium's isotope, ^{7}Li is often used in LIB neutron studies as it has an absorption cross section of 0.045 barns.

3. Application of neutron techniques on NIB cathode material investigation

3.1. Sodium metal oxides

3.1.1. Sodium cobalt oxides

In NIB research, sodium cobalt oxides (Na_xCoO_2) have been the most obvious first choice as cathode material candidates, due to similarities to their LIB cathode counterparts. In the following studies mentioned, NPD and QENS methods have been employed to reveal crystal structures, distinguish particular phases, and investigate Na$^+$ ion diffusion within these cathode materials.

Beck *et al* [22] studied an as-made cathode material, NaCoO$_2$, which can exhibit four different structural phases. Its P2 phase is the most common, where P corresponds to the trigonal prismatic coordination sites at which Na$^+$ ions are located, and the numeral denotes the number of layers in its unit cell. XRD results confirmed the P2 type structure where Na$^+$ ions reside in trigonal prismatic sites between the CoO$_2$ layers allowing for Na$^+$ ion mobility. A manganese substituted cobalt oxide, $Na_{0.79}[Co_{0.7}Mn_{0.3}]O_2$, was also prepared and NPD was used to distinguish between Co and Mn. It was found that the Mn atoms were substituted onto the Co sites and this type of substitution led to an increase in the *c*-direction of the lattice while the spacings in the *a*-direction remained unchanged. This characterisation method was a valuable use of neutrons since Co and Mn have similar atomic numbers and therefore would be difficult to distinguish using x-rays. Electrochemical analysis of half-cells against Na metal showed similar behaviour for both materials, suggesting that the Mn-substituted material provides a cheaper and more sustainable alternative as it uses less Co [22].

Na_xCoO_2 $(0.2 \geqslant x \geqslant 1)$ has actually been studied since the early 2000s for its ferroelectronic and superconductor properties. A number of studies have shown that varying the stoichiometric amounts of sodium affords different structural phases of the material. For example, Viciu *et al* [23, 24] found that when $x = 0.92$ and 0.32, an O3 structure (where Na ions reside in octahedral sites) was observed and when $x = 0.2$ and 0.51, a P1 structure was identified through NPD. Huang *et al* [43] observed two distinct structural phases of Na_xCoO_2 when $x = 0.75$, where Na$^+$ ions occupy different sites. A high symmetry structure was converted

to a lower symmetry structure upon only heating from 20 °C to 50 °C. Another study of a sample with similar stoichiometry, where $x = 0.7$, also observed the same structural change but at a higher temperature of 130 °C through high resolution NPD [44]. Although these studies gave useful information regarding the various phases associated with certain sodium contents, the materials were not electrochemically tested and therefore their capabilities as NIB cathodes are unknown. Electrochemical characterisation is necessary to identify which stoichiometries and phases give rise to superior performances as NIB cathodes.

In a QENS study [45], Na$_{0.7}$CoO$_2$ was found to exhibit temperature dependent changes in inelastic and elastic intensities at $T_A = 15$ °C and $T_B = 130$ °C. Small changes in the phonon density of states (PDOS) at both T_A and T_B were assigned to Na$^+$ ion vibrations caused by structural changes. Slight quasi-elastic scattering above T_A was attributed to these low energy vibrations. Na$^+$ ion quasi-elastic scattering clearly became visible above T_B, and a computed diffusion coefficient of 5×10^{-10} m^2 s^{-1} was attributed to 2D isotropic diffusion despite poor Q dependent statistics. The correlation between localised diffusion onset and appearance of low energy phonons above T_B suggest coupling between lattice vibrations and Na diffusion. The diffusivity from QENS was four orders of magnitude greater than muon spin relaxation (μSR) and NMR spectroscopy studies. The authors logically attributed this difference to two distinct motions within Na$_{0.7}$CoO$_2$; a fast localised type on the order of 50 ps (from Q independent QENS), and slower long range translational diffusion (from μSR and NMR).

Na$_{0.8}$CoO$_2$ was studied by Willis *et al* [46] who also linked the structural and dynamic transitions at different temperatures. It is understood that anomalous mobility of specific Na sites is due to rattling of ions in tri-vacancy clusters above −90 °C. XRD revealed a low temperature, fully ordered superstructure comprising stripes of tri-vacancy clusters that became partially disordered above 15 °C and a mixture of di-, tri- and quadri- vacancy clusters above 95 °C. *Ab initio* MD (AIMD) simulations showed the interconnected tri-vacancy clusters in the ideal striped arrangement with hopping between 2b and 2d sites perpendicular to stripes, leading to tri-vacancy translation but no net Na diffusion. An increase in the quasi-elastic intensity observed on formation of the partially disordered stripe structure suggested an additional vacancy on a 2b site. This led to a sequence of hops providing a 1D diffusion channel along stripes with $E_a = 170$ meV. At 25 °C, a mean residence time of 490 ps gave a diffusion coefficient along the quasi-1D diffusion channels of 1.4×10^{-7} cm^2 s^{-1}. The fully disordered phase (>95 °C) showed 2D superionic diffusion with $E_a = 85$ meV. A successful fit of the Q-dependence with the CE model of jump diffusion with hopping distance fixed to the 2d to 2b separation confirms the 2d to 2b hops to be the dominant diffusional process in both dynamic phases. This information not only supports, but gives further insights into the phase transitions observed in the previous studies of these materials [43, 44].

3.1.2. Sodium nickel/titanium oxides

Many other metal oxides have been of interest as alternatives for Co-based electrodes to reduce their cost. For example, nickel and titanium metals are not only cheaper than cobalt but are also of similar size, and therefore could exhibit comparable capacities to Co-based cathodes. In the following cases, NPD of an as-made Ni-based oxide revealed its local structure [47], while elsewhere, QENS was used to give insights on the diffusive motions of a Ti-based oxide [48].

Ma *et al* [47] synthesised Na[Ni$_{2/3}$Sb$_{1/3}$]O$_2$ at two temperatures; 1000 °C and 1200 °C and labelled the 'low' and 'high' temperature products as disordered and ordered, respectively. NPD was used for local structure analysis which suggested that both samples had no disorder in the *a*-direction while XRD results showed disorder in the *c*-direction only for the 'low' temperature product, arising from stacking faults in its structure. Electrochemical performances of the materials were similar; a fairly stable capacity was observed at ∼125 mA h g^{-1} for the ordered product and a less stable capacity of ∼105 mA h g^{-1} for the disordered product at 4 mA g^{-1} rate. Both materials displayed poor capacities at faster rates. The authors suggested that the lower capacity for the disordered material may be explained by the presence of trapped regions of Na$^+$ ions arising from stacking faults. However, this theory seems unlikely with such a small capacity difference between the two materials. The disordered material also had lower capacity retention (70% vs 90% for the ordered material by the 25th cycle), which could be a more likely consequence of the stacking faults, but this theory can only be validated by post cycling structure analysis.

In a study of Na$_{2/3}$[Ni$_{1/3}$Ti$_{2/3}$]O$_2$, broadening of the QENS spectra was observed between 180 °C and 230 °C [48]. The continuous translational (Fickian) self-diffusivity of Na extracted from $\Gamma = DQ^2$ in this temperature range was on the order of 10^{-6} cm^2 s^{-1} with an $E_a = 150$ eV, and a diffusivity of ∼10^{-7} cm^2 s^{-1} at room temperature. The low activation energy barrier of this material is comparable to Na$_{0.8}$CoO$_2$ (170 meV at 80 °C) [46]. Deviation from $\Gamma = DQ^2$ at smaller distances suggested localised jump behaviour, described by the SS jump model with jump lengths between 1 and 1.8 Å. This jump length matched well with edge-sharing and nearest-neighbour face-sharing sites (1.7 Å), suggesting primary migration through a 2D
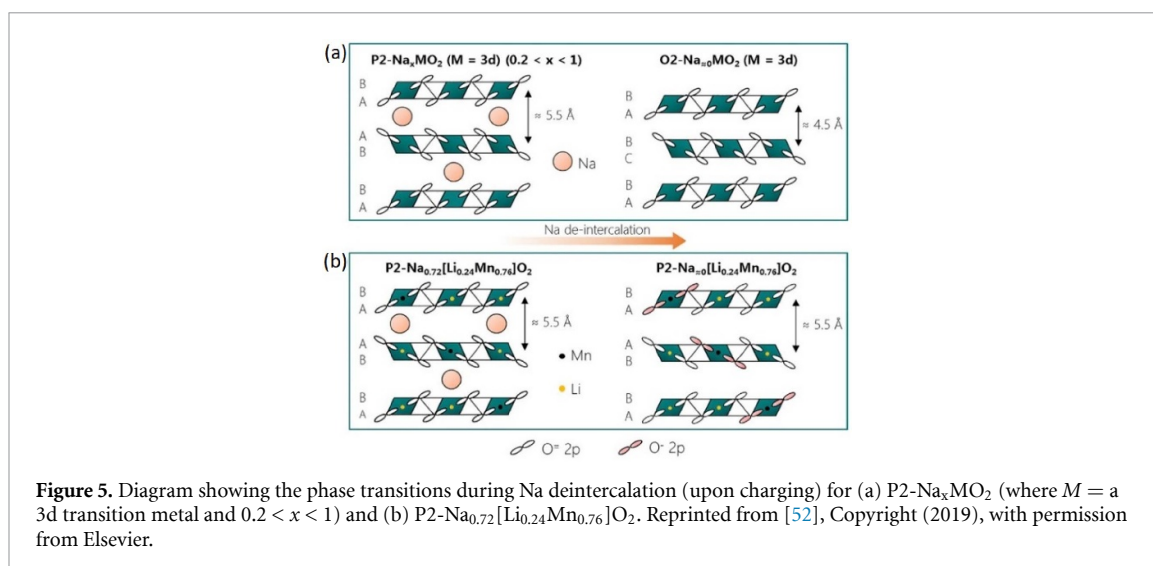
diffusion pathway. DFT also suggested a 2D honeycomb diffusion pathway in the Na layer with no cross-plane diffusion, but with self-diffusivity and E_a about two times higher. Na^+ diffusivity of a Na-deficient phase, $Na_{5/9}[Ni_{1/3}Ti_{2/3}]O_2$, and a Na-rich phase, $Na_{7/9}[Ni_{1/3}Ti_{2/3}]O_2$, was modelled to examine the electrochemical performance of the material upon cycling. The Na-deficient phase showed comparable Na^+ diffusivity, whilst the Na-rich phase had a significant diffusivity drop compared to the pristine phase, due to a limited number of vacancies. However, both phases had higher ionic conductivity due to increased vacancies or charge carriers, respectively.

3.1.3. Sodium manganese oxides substituted/inserted with metals

Mn-based electrodes are another class of sodium metal oxides that have been widely studied as NIB cathode materials due to their high theoretical capacities [49]. However, many studies have highlighted their poor practical cycling retentions, resulting from unfavourable phase changes of the materials. Upon the first charge (Na deintercalation), it is understood that the materials undergo a phase transition from P2 to O2 as the concentration of Na^+ ions becomes low [50, 51]. The initial removal of Na^+ ions reduces the interlayer distance between MO_2 layers, but further removal induces repulsive forces between the layers since there are not enough Na^+ ions to stabilise the P2-type stacking. As a result, the MO_2 layers glide and the structure collapses, forming an O2 phase in the process (as shown in figure 5(a)). Upon discharge, as Na content increases, the reverse phase change occurs. These phase changes cause continuous volume expansion and contraction upon cycling which eventually lead to cracking in the electrode material, reducing its cycle life. To supress this unfavourable phase transformation, researchers have attempted to dope Mn-based oxides with magnesium and lithium (as illustrated in figure 5(b)) [52–57] or substitute some of the Mn for different transition metals [58, 59].

Han *et al* [58] synthesised a Fe- and Ti-substituted Mn oxide material, P2-$Na_{2/3}[Mn_{0.8}Fe_{0.1}Ti_{0.1}]O_2$, in the hope to eliminate the undesirable P2–O2 phase transformation that occurs for Na_xMnO_2 during electrochemical cycling. The cathode achieved a reversible capacity of $\sim$140 mA h g^{-1} at 25 mA g^{-1} rate for 50 cycles with a capacity retention of 95%. Although a P2–O2 transformation was not observed in the *in situ* XRD experiment during the first two cycles, a new phase appeared towards the end of the first discharge around 2.2 V vs Na. The authors describe this phase as a distorted P2 structure, denoting it as P'2. The P'2 phase did however completely disappear upon the second charge process and the original P2 peaks were observed. From these findings, it is likely that the unfavourable phase change was avoided but a new, reversible phase change occurred. The same group later formed Ni- substituted versions of this material, P2-$Na_{2/3}[Mn_{0.9-x}Ni_xFe_{0.05}Ti_{0.05}]O_2$ (where $x = 0.1$ and 0.2) [59]. Since NPD is sensitive to the ordering of Mn and Ni (due to their differing neutron scattering lengths), it was used to determine their Mn-site occupancies. It was found that Ni occupies one transition metal site when $x = 0.1$ and two when $x = 0.2$. The material with less Ni gave a slightly better electrochemical performance with a reversible capacity of $\sim$160 mA h g^{-1} compared to $\sim$130 mA h g^{-1} for the higher Ni content at 2.4 mA g^{-1} rate for 50 cycles. This finding suggests that an optimum amount of Ni may achieve the highest possible capacity, and a simple systematic study of a wider range of Ni stoichiometries could confirm this theory. Also, their capacity retentions were similar and the only difference in the *in situ* XRD was that the P'2 phase remained for a longer duration for the higher Ni content sample. This implies that although the disordered P'2 phase is reversible during cycling , it is still detrimental, although to a lesser extent, than the O2 phase.

Clément *et al* [54] studied the effect of doping P2-$Na_{2/3}MnO_2$ with different amounts of Mg, P2-$Na_{2/3}[Mg_xMn_{1-x}]O_2$, where $x = 0$, 0.05 and 0.1. *Ex situ* NPD and XRD characterisation techniques were used to observe the structural changes between the as-made, charged (Na-deintercalated by charging to 1.8 V vs Na), and discharged (Na-intercalated, by discharging to 3.8 V vs Na) samples. Here, neutrons enabled a more accurate picture of the material structures owing to the increased sensitivity of neutrons to Na in the measured diffraction patterns. They found that the undoped material, $Na_{2/3}MnO_2$, fully transforms into an OP4 phase at the end of charge, consisting of alternating trigonal prismatic and octahedral layers. Upon discharging, NPD showed that the reverse transition occurs as the P2 phase reappears at the end of discharge. This behaviour was in contrast to the doped materials as their compositions at the end of charge remained mostly in the P2 phase. Further electrochemical analysis supports these findings as the charge–discharge curves for the doped samples were much smoother than the undoped, implying fewer or smaller structural changes. Additionally, doping enhanced the cycling stabilities and it was suggested that Mg substitution delayed the MO_2 layers from gliding, allowing only partial phase transformation to take place, which was more reversible than the changes that occurred in the undoped sample. Tapia-Ruiz *et al* [53] studied a similar compound, P2-$Na_{2/3}[Ni_{1/3-x}Mg_zMn_{2/3}]O_2$, with varied Mg contents where $x = 0$, 0.05, 0.1, and 0.2. NPD peaks of the as-made materials were similar for the samples with 0%, 5%, and 10% Mg content, suggesting that the Mg^{2+} ions sit in the same octahedral sites as the Ni^{2+} ions, and therefore maintain the P2 structure.

Figure 5. Diagram showing the phase transitions during Na deintercalation (upon charging) for (a) P2-Na$_x$MO$_2$ (where M = a 3d transition metal and $0.2 < x < 1$) and (b) P2-Na$_{0.72}$[Li$_{0.24}$Mn$_{0.76}$]O$_2$. Reprinted from [52], Copyright (2019), with permission from Elsevier.
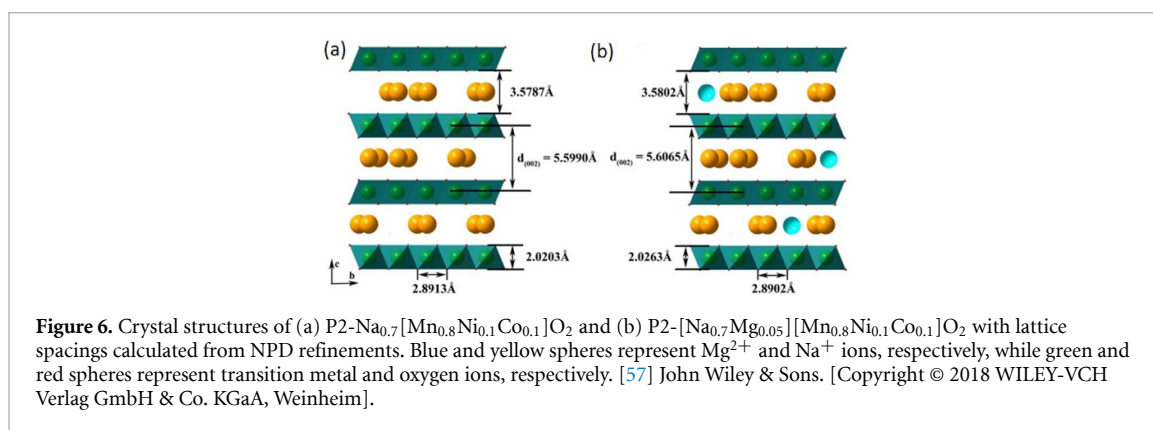
Operando synchrotron XRD indicated that Mg doping prevented the formation of the unfavourable O2 phase but induced an OP4 phase transformation instead at higher voltages. This finding supports the study by Clément *et al* [54], where MO$_2$ layer gliding is delayed due to the higher average oxidation state of Mn as a result of Mg substitution.

More recently, Rong *et al* [52] synthesised and electrochemically tested a lithium substituted manganese oxide material, P2-Na$_{0.72}$[Li$_{0.24}$Mn$_{0.76}$]O$_2$, which was found to exhibit the highest practical capacity to date, for a NIB cathode, of $\sim$270 mA h g^{-1} at 10 mA g^{-1} rate over 30 cycles. They claimed that the improved cycling stability was a direct result of Li doping which prevents phase transformation to either O2 or OP4 structures, as indicated by *in situ* XRD experiments. Moreover, nPDF patterns of the pristine, charged, and discharged samples showed that the P2 packing structure was maintained. nPDF results also highlighted the shortening of the O–O interlayer distance after Na-deintercalation, which suggests the occurrence of a redox reaction on the oxide anions. The authors confirmed this theory by using x-ray absorption spectroscopy to probe the oxidation state of the oxygen anions, where *ex situ* studies showed pre-edge peak shifts between the charged and discharged samples. These findings suggested a reduction in the negative charge of the oxide ions which, in turn, reduces the repulsive forces between the metal oxide layers when Na is extracted, allowing a stabilised P2 phase to be maintained upon cycling, as depicted in figure 5(b) [52, 55]. We believe that the authors of this study postulated logical theories regarding the origins of the impressive capacities, which were also supported by additional characterisation. Another Li-substituted sample, P2-Na$_{0.8}$[Li$_{0.12}$Ni$_{0.22}$Mn$_{0.66}$]O$_2$, was studied by Xu *et al* [60], and was found to exhibit similar behaviour to the Mg-substituted samples where the O2 phase was delayed rather than completely prevented. NPD was used to identify the as-prepared P2 phase and slight changes in *a* and *c* lattice parameters were tracked by *in situ* synchrotron XRD during the first charge between 2.0 and 4.4 V vs Na. This suggests that the substituted Li allows for enough Na$^+$ ions to remain within the structure up until 4.4 V vs Na and therefore suppresses the P2–O2 phase change.

In the previously discussed studies, alkali metals are substituted onto transition metal sites which maintains the P2 structure. A different approach to eliminate unfavourable phase changes is to substitute alkali metals onto the alkali site instead and afford an O3 structure. This was achieved by Wang *et al* [56] via synthesising O3-[Na$_{0.67}$Li$_{0.2}$][Fe$_{0.4}$Mn$_{0.4}$]O$_{1.6}$. Synchrotron XRD and NPD patterns confirmed substitution into the alkali metal site but also indicated a smaller interlayer spacing from a reduction of the *c* lattice parameter, compared to O3-Na$_{0.67}$[Fe$_{0.5}$Mn$_{0.5}$]O$_2$. The Li-substituted material showed superior electrochemical performance with initial capacity of $\sim$160 mA h g^{-1} at 10 mA g^{-1}, and a capacity retention of 81% after 100 cycles, while O3-Na$_{0.67}$[Fe$_{0.5}$Mn$_{0.5}$]O$_2$ started at $\sim$120 mA h g^{-1} with a capacity retention of 34%. *In situ* synchrotron XRD gave insights into this superior stability as an O3–P3–O3 phase transformation was observed during the first and second cycles. This transformation does not include the detrimental O2 phase which is possibly the reason for the improved capacity retention.

Instead of substitution, another group incorporated Mg$^+$ ions into the Na$^+$ ion layers and formed P2-Na$_{0.7}$Mg$_{0.05}$[Mn$_{0.8}$Ni$_{0.1}$Co$_{0.1}$]O$_2$ (figure 6) [57]. Compared to the material without Mg, an increase in the interlayer spacing was observed in XRD and NPD patterns, which the authors interpret as likely due to the larger size of Mg. The Mg-substituted material also showed better capacity retention. It was persistently

Figure 6. Crystal structures of (a) P2-Na$_{0.7}$[Mn$_{0.8}$Ni$_{0.1}$Co$_{0.1}$]O$_2$ and (b) P2-[Na$_{0.7}$Mg$_{0.05}$][Mn$_{0.8}$Ni$_{0.1}$Co$_{0.1}$]O$_2$ with lattice spacings calculated from NPD refinements. Blue and yellow spheres represent Mg^{2+} and Na$^+$ ions, respectively, while green and red spheres represent transition metal and oxygen ions, respectively. [57] John Wiley & Sons. [Copyright © 2018 WILEY-VCH Verlag GmbH & Co. KGaA, Weinheim].

claimed by the authors that the increased interlayer spacing and 'unique football-like hierarchical' structure were the reasons for the improved capacity retention. However, material characterisation studies were not performed during or after electrochemical analysis, therefore we believe that it is not possible to make this claim regarding the origins of the electrode's enhanced stability. *In situ*, *operando* or simply *ex situ* studies before and after cycling would have given more insight into these findings.

It is evident from these studies that the nature of some phases, and phase transitions that ensue, often hinder the ability of sodium metal oxides to perform well in a battery. Doping with guest ions usually enhances the overall capacity and capacity retention, yet the exact determinant of these improvements is still unclear. Identifying the voltages associated with the onset of phase transitions using *operando* neutron experiments could provide more information about the true origins of the increased capacity. Once the origins are established, further improvements considering the material can be made, such as the nature or the amount of dopant.

3.2. Sodium metal phosphates

Phosphate-based compounds are polyanionic insertion cathode materials and are also under study for NIBs. Although their theoretical capacities are lower than sodium metal oxides due to the large polyanions, they often maintain superior operating voltages and therefore achieve similar energy densities. Additionally, sodium metal phosphates retain high stability over a wide range of temperatures. In this section, various sodium metal phosphate studies are discussed where NPD was employed on as-made materials in most cases and two *ex situ* cases to reveal structure changes after electrochemically cycling.

Kim *et al* [61] synthesised Na$_4$Fe$_3$(PO$_4$)$_2$(P$_2$O$_7$) and a desodiated phase, NaFe$_3$(PO$_4$)$_2$(P$_2$O$_7$), which was achieved by adding a strong oxidising agent. The NPD and XRD patterns showed no significant changes between the sodiated and desodiated samples, which led the authors to infer that Na$^+$ ions deinsert in a topotactical manner without any distortion to the material components. However, one year later, the same group [62] published *ex situ* NPD and XRD patterns after electrochemically charging the as-made material to form the desodiated compound and found that the (P$_2$O$_7$) polyhedrons reversibly distort upon cycling. This is a prime example of the necessity for *ex situ* experiments since the material behaved differently during chemical desodiation and electrochemical desodiation. Only a 4% change in the unit cell volume was observed after chemical desodiation, and the as-made material showed good cycling stability of 110 mA h g^{-1} capacity at 6.5 mA g^{-1} rate for the first 20 cycles.

Shinde *et al* [63] synthesised a similar compound without the (P$_2$O$_7$) polyhedrons, Na$_3$Fe$_3$(PO$_4$)$_4$, but found that it gave a very poor practical capacity upon cycling of ∼50 mA h g^{-1} at 2.6 mA g^{-1} for the first ten cycles. Using DFT, they also performed bond valence site energy calculations and found that Na$^+$ ion diffusion occurs along a 1D pathway along the (101) plane albeit with a high energy barrier. This energy barrier could explain such low capacity during cycling. An earlier report included a similar material substituted with Mn, NaMnFe$_2$(PO$_4$)$_3$ [64]. In this case, XRD data revealed two distinct transition metal sites, M1 and M2, but could not distinguish their occupancy regarding Mn and Fe since these metals have similar x-ray scattering atomic factors. NPD data, on the other hand, was able to reveal that Mn was mainly located in M1 and Fe in M2. The material was tested as a cathode in both Na-ion and Li-ion half-cells and exhibited capacities of ∼75 and ∼85 mA h g^{-1}, respectively in the first cycles.

Na superionic conductor (NASICON) type structures are currently being studied as SSEs for all-solid-state NIBs; however, they were previously proposed as cathodes for conventional NIBs. Na$_3$V(PO$_4$)$_2$ is an example that was studied by Liu *et al* [65], hoping to utilise the multivalent nature of vanadium

(V^{3+}/V^{4+}/V^{5+}) to enhance capacity. Rietveld refinement of XRD and NPD were carried out and combined to confirm the structure, bond lengths and angles. X-ray absorption near edge structure spectroscopy was used to identify the V^{3+} oxidation state in the as-made material. Although the material exhibited low capacity (~70 mA h g^{-1} at 8.7 mA g^{-1} rate), it showed good stability in the voltage range 2.5–3.8 V vs Na, yet the V^{4+}/V^{5+} couple was only activated when charged to 4.2 V vs Na. Initially, a higher capacity was observed in the higher voltage range but its cycling performance was much poorer. We believe that the low cycling stability possibly stemmed from a large volume expansion or unfavourable phase change, yet the lack of *operando* or *ex situ* post cycling electrode analysis makes this theory difficult to uphold. A similar NASICON material, $Na_3V_2(PO_4)_2F_3$ [66], was found to exhibit a much higher capacity and exceptional cycling stability of ~110 mA h g^{-1} at 12.8 mA g^{-1} for 30 cycles in the higher voltage range and therefore managed to activate the V^{4+}/V^{5+} redox couple, without causing substantial strain in the structure. XRD and NPD analyses of the as-made material were in good agreement in identifying the preference of Na^+ ions occupying trigonal prismatic sites. This finding was further supported by DFT results which predicted only small changes in the lattice parameters upon sodiation and desodiation, suggesting that substantial phase changes did not occur. Comparing this material with the NASICON synthesised by Liu *et al* [65], it is likely that the substitution of octahedral $V_2O_4F_2$ units for tetrahedral PO_4^{3-} anions allowed for a more stable structure to form while the higher oxidation states of vanadium were achieved.

Building on from this work, Muruganantham *et al* [67] completed a systematic study of $Na_3V_2(PO_4)_3$ doped with different amounts of F$^-$ ions, $Na_{3-x}V_2(PO_{4-x}F_x)_3$, where x = 0, 0.1, 0.15, and 0.3. XRD patterns showed a slight increase in the *a* lattice constant for the doped samples compared to the pristine sample. The larger anionic radius of the F anion than that of V and Na cations were suggested for this observation. NPD confirmed that the sites that were fully occupied by oxygen in the pristine sample were partially occupied by F$^-$ ions in the doped samples. Out of the doped samples, the best electrochemical performance was achieved when x = 0.15, with a reversible capacity of ~100 mA h g^{-1} at 0.1 A g^{-1} rate for 250 cycles. However, when x = 0.1 and 0.3 the capacities were lower than that of the undoped material, suggesting that x = 0.15 was an optimum amount.

Materials with two types of polyanion units have also been considered as cathodes for NIBs. For example, Kan *et al* [68] synthesised $Fe_3P_5SiO_{19}$, which contains both PO_4^{3-} tetrahedra and $Si_2O_7^{6-}$ octahedra. They also synthesised its sodiated form, $Na_{0.7}Fe_3P_5SiO_{19}$, via chemical sodiation. Bond lengths and angles were analysed by refinement of powder XRD and TOF NPD of the as-made and sodiated materials, both of which showed no significant changes in their diffraction patterns. This suggests that $Fe_3P_5SiO_{19}$ does not undergo any phase changes when uptaking Na^+ ions. NPD also revealed that Na^+ ions are disordered in the structure. To study its electrochemical properties, $Fe_3P_5SiO_{19}$ was discharged first, producing a sodiated form, $Na_xFe_3P_5SiO_{19}$, affording an initial capacity of only ~70 mA h g^{-1} which equates to ~1.7 Na^+ ions per formula (theoretically, three Na^+ ions should sodiate per formula as all three Fe^{3+} ions should reduce to Fe^{2+} ions). Stable cycling was achieved after the first cycle capacity loss to ~60 mA h g^{-1} up to 30 cycles [68]. A stable cycling performance may imply that no phase changes occurred, which is also supported by the diffraction patterns of the chemically sodiated material. However, we have found earlier that a chemically sodiated material may not behave in the same way to electrochemical sodiation [61, 62], therefore we cannot directly link the findings of the two methods in this case. Although this capacity is much lower than other NIB cathode materials under study, its characterisation could aid the search and synthesis of NIB SSEs.

From the research mentioned, it is clear that a range of cathode materials, including cobalt and manganese oxides, their doped versions, phosphate-based compounds, and NASICON-type materials, have been studied using neutrons. However, these studies are mainly of the as-made materials or of their chemically sodiated/desodiated forms. Only two papers [54, 62] performed *ex situ* NPD experiments after electrochemically testing their materials, and therefore were able to provide informed theories on the type of mechanisms occurring during electrochemical charging and discharging. Only speculations on the underlying mechanisms could be made by the other papers due to the lack of post cycling analysis of their materials. Moreover, the low capacities and capacity fading in NIB cathode materials highlights the requirement of, at minimum, *ex situ* neutron studies of these materials post cycling to understand the mechanistic reasons behind their performances. QENS studies showed that different Na amounts in Na_xCoO_2 possess vastly differing diffusion properties and therefore are not necessarily representative of electrode properties throughout cycling operation. The possibility to study cathode materials at various states of charge and to observe differing ion dynamics of degraded samples may also reveal degradation mechanisms that limit electrode cyclability.

## 4. Application of neutron techniques on NIB anode material investigation

4.1. Carbons

Most of the recent research into finding alternatives to graphite for use in NIB anodes considers HCs, due to their various sodium ion storage sites discussed in section 1.1. In contrast to most crystalline cathode materials, HCs give rise to broad peaks that are difficult to interpret in their NPD patterns due to their amorphous structures. For this reason, total neutron scattering is employed for studying HCs, and SANS in particular is usually the method of choice for extracting average pore sizes. Additionally, total neutron scattering can provide information regarding all pores within the structure, including pores that are inaccessible to gas adsorption characterisation methods such as Brauner–Emmett–Teller (BET).

HCs are often synthesised by annealing non-graphitisable carbons at high temperatures. Titirici *et al*'s group [15, 69] synthesised a range of HCs by heating glucose at different pyrolysis temperatures. Simultaneous SANS and neutron total scattering on the NIMROD instrument at ISIS [70] was then used to characterise these samples at the atomic and mesoscale. SANS data revealed that higher temperature synthesis led to larger average pore sizes. Analysis of the higher Q diffraction data and its Fourier transform to the pair distribution function, $g(r)$, allowed this increase in pore size to be correlated with increased graphite domain size (from Scherrer analysis of diffraction peak and the distance at which $g(r)$ goes to zero), increased graphitisation from increased number of 6 membered carbon rings (from $g(r)$), and shorter interlayer spacings (from the 002 diffraction peak position). Figure 7 highlights changes in scattering at low Q ($Q < 0.8$ Å^{-1}) for the different pyrolysis conditions. This region in Q-space corresponds to length scales of $\sim$1–30 nm, and can therefore identify changes in the pore structures. The pore sizes were corroborated by BET methods with N_2 and CO_2 gas adsorption techniques, though, as mentioned above, it should be noted that such adsorption methods will not reveal information on the inaccessible pores inside the HC that nevertheless can contain sodium clusters upon electrochemical sodiation. Upon electrochemical testing, they found that increasing the carbonisation temperatures during synthesis, and therefore pore size, reduced the specific capacities but increased the percentage contribution of the plateau region to the total capacity. These findings further support the theory that the plateau region corresponds to sodium ion storage via pore filling, since the larger pores allowed for more sodium to be stored.

Bommier *et al* [19] annealed sucrose also at different temperatures (1100 °C, 1400 °C, and 1600 °C) and the product structures were analysed with various characterisation techniques. Total neutron scattering and PDF results showed no differences in C–C distances between the different annealing temperatures and no C–C correlation between 3.35 and 3.45 Å, which is usually found for graphitic carbons. Discharge curves showed a higher voltage for the onset of sodiation in the sloping region of the sample annealed at 1100 °C, compared with that of the samples annealed at higher temperatures. PDF and Raman spectroscopy indicated more defects in this sample and therefore it was suggested that the defect sites have higher Na$^+$ ion binding energies thus requiring higher voltages to overcome, which is in agreement with other literature [8]. The authors also suggest further intercalation of Na$^+$ ions into the TNDs towards the end of the plateau region between 0.2 and 0.01 V vs Na [19], however, this assumption has been highly disputed by other research [8, 15, 17, 69].

The HC pyrolysed at 1100 °C was later compared with soft carbons derived from an organic solid of perylene tetracarboxylic dianhydride pyrolysed at 900 °C [71]. In contrast to HCs, soft carbons are graphitisable where some regions contain graphene sheets stacked in a more or less parallel form. This gives rise to a larger sloping region for soft carbons compared to HCs but smaller than graphite. Total neutron scattering with PDF analysis was used to determine the level of local defects in these materials. The $g(r)$ peak amplitudes beyond the nearest neighbours in the hexagonal graphene unit were smaller for the soft carbon compared to the HC, indicating a more defective nature for the soft carbon. Their findings were argued to support the theory that the sloping region capacity includes Na$^+$ ion storage on defective sites, as the reversible sloping capacity for their soft carbon was $\sim$195 mA h g^{-1} compared to $\sim$150 mA h g^{-1} for the HC. Li *et al* [72] further tested the defect-slope capacity correlation by introducing defects through low temperature (650 °C) synthesis of cellulose filter paper, LT-HC. The resulting LT-HC had smaller $g(r)$ peak amplitudes than that of the same precursor pyrolysed at 1100 °C (HT-HC), suggesting more defects in the LT-HC product. A sloping capacity of $\sim$30 mA h g^{-1} was observed for LT-HC, yet HT-HC had a larger total capacity, which arose from its plateau capacity.

The same group also showed that doping HC with certain elements increases the overall capacity. P-, B- and S-HCs were synthesised using phosphorus, boron and sulphur containing oxo-acids, respectively. XRD patterns of P- and S-HCs had increased *d*-spacings, while that of the B-HC remained similar to the undoped HC. Again, total neutron scattering and associated PDF analysis were employed, revealing a reduction in the $g(r)$ peak intensity for each of the doped HCs, indicating a more defective structure along the *ab* planes. The
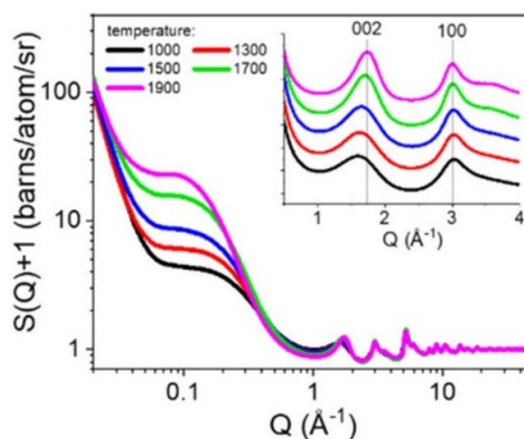
Figure 7. SANS of HCs pyrolysed at different temperatures. Reprinted with permission from [69]. Copyright (2020) American Chemical Society.
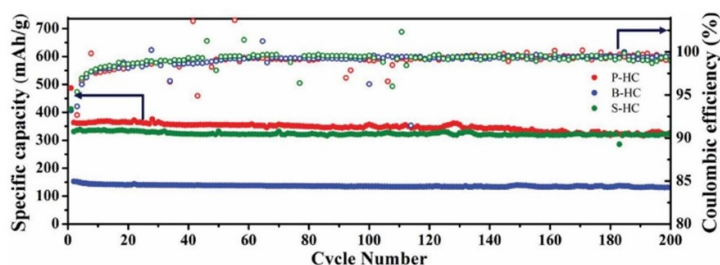
Figure 8. Electrochemical performances of P-, B- and S-doped HC in HC/Na half-cells at 20 mA g^{-1} current rate. [76] John Wiley & Sons. [Copyright © 2017 WILEY-VCH Verlag GmbH & Co. KGaA, Weinheim].

electrochemical performances of both P- and S-HCs showed high and stable capacities of ∼350 and ∼325 mA h g^{-1}, respectively, while B-HC material exhibited a much lower capacity of ∼150 mA h g^{-1}, as shown in figure 8. In its cyclic voltammogram, a sharp cathodic peak was observed indicating sodiation, yet a broad anodic peak was observed in the reverse scan, suggesting that the Na$^+$ ions are strongly bound and difficult to remove. This study implies that doping HC with elements that do not have a strong affinity to Na$^+$ ions enable higher capacities. Another theory proposed by the authors for the increased capacities was due to higher defect levels for S- and P-HCs which were identified by PDF. However, Raman spectroscopy did not support this argument as it suggested that the undoped HC had a higher defect level than S-HC (by considering I_D/I_G ratios) [73, 74]. Moreover, neither technique can identify the specific nature of the defects present, therefore it is difficult to determine which defects enhance or hinder the capacity. Consequently, we recommend the use of x-ray photoelectron spectroscopy which could provide complementary information by analysing the different carbon bond types to deduce the nature of the defects.

Wu *et al* [75] studied commercial Super-P carbon, a spherical, porous carbon which is often used as a conductive additive in electrode synthesis. An initial capacity of ∼250 mA h g^{-1} dropped to ∼100 mA h g^{-1} by its second cycle, presumably due to large solid electrolyte interphase (SEI) formation. However, *ex situ* analyses of the electrode suggested another possibility. High resolution transmission electron microscopy (TEM) with selected area electron diffraction showed Na metal within micropores after initial electrochemical sodiation and after desodiation. An increased graphite interlayer spacing from 3.57 to 4.41 Å after sodiation also remained after desodiation as suggested by poorly defined, broad peaks in the NPD results. Despite the poor definition of the peaks, they are in agreement with the TEM findings which suggests that the irreversible capacity loss originated from irreversible formation of Na metal clusters in micropores during sodiation.

4.2. Sodium titanates
Sodium titanates have also been considered as possible anode materials for NIBs due to their low intercalation potentials and small volume changes upon cycling [76]. These properties are highly

advantageous since anode materials with lower intercalation potentials exhibit higher energy density, while a stable volume during operation often leads to higher cycle life.

Ma *et al* [77] synthesised a novel sodium titanate compound, $NaAlTi_3O_8$, and analysed its structure and electrochemical performance. Rietveld refinements of both XRD and neutron diffraction indicated a tunnel framework where Na^+ ions can easily intercalate and deintercalate. Considering a redox reaction for all three titanium ions from Ti^{4+} to Ti^{3+} and the formation of $Na_4AlTi_3O_8$, a theoretical capacity of 250 mA h g^{-1} would be expected, yet their material showed a much lower stable reversible capacity of ~65 mA h g^{-1} for 100 cycles. This measured capacity corresponds to the sodiation/desodiation of ~0.75 Na^+ ions. There was a significant drop in capacity between the first discharge and charge of ~140 mA h g^{-1}. SEI formation could explain the drop in capacity and the loss of Na inventory. *In situ* and *ex situ* XRD patterns of the material at various states of discharge indicated no phase transitions taking place and slight shifts in the *a*- and *c*-directions were assigned to Na^+ ions taking a solid solution-like phase pathway during intercalation and subsequent deintercalation. This finding further supports the theory that SEI formation on the surface of the material was the main cause of such low capacity.

Another group [78] synthesised a chemically desodiated titanate, $H_2Ti_3O_7$, via ion exchange of Na^+/H^+. They took neutron diffraction patterns at two different wavelengths ($\lambda = 1.28$ Å and $\lambda = 2.52$ Å) to refine the distinct hydrogen positions within the structure and their occupancies. The higher neutron wavelength is more sensitive to low angle reflections and therefore was able to identify three hydrogen positions instead of only two that were identified in a previous study [79]. *In situ* PXRD showed slight shifts in reflections until 0.6 mol of sodium was inserted, indicating initial intercalation formed a phase where both Na^+ and H^+ ions coexist in the interlayer spacing. Further insertion of Na^+ ions gave rise to new reflections in its PXRD pattern, implying that beyond a certain amount of Na, the extra Na causes gliding of the layers and induces a phase change. It was found that electrochemically cycling at a low voltage range (0.05–1.6 V vs Na) after two initial cycles at a high voltage range (0.9–2.2 V vs Na) gave the best performance of 130 mA h g^{-1}. The authors used *ex situ* ^{1}H-NMR to confirm that most of the H^+ ions were removed in the two initial cycles at the high voltage range and only 0.2 mol H^+ per unit formula remained by the end of the second cycle. Naeyaert *et al* [80] synthesised a monoclinic form of $Na_4Ti_5O_{12}$ which had previously been tested as a NIB anode material in its trigonal form [81]. NPD revealed partially occupied Na sites for the monoclinic phase, in contrast to the fully occupied sites of the trigonal phase. Partially occupied sites suggest the ability for more Na^+ ions to intercalate and therefore a larger capacity would be likely. However, the materials had similar reversible capacities of ~60 and ~50 mA h g^{-1} for the monoclinic and trigonal phases, respectively, which equates to intercalation of about 1 Na^+ ion.

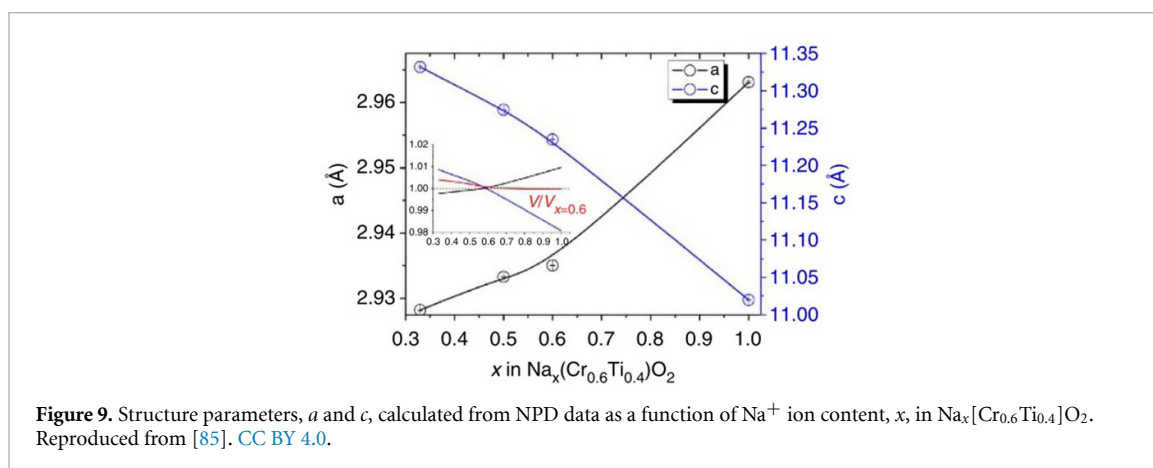Ma *et al* [82] investigated an oxyfluorinated titanium phosphate material, $Na_3[Ti_2P_2O_{10}F]$, using neutron diffraction at a range of temperatures to visualise the Na^+ ion diffusion path within the structure. *Ex situ* neutron diffraction experiments were conducted from room temperature to 600 °C at various temperatures and no structural transition was observed in this temperature range. Considering the absence of Na scattering through the layers within this temperature range, NPD data suggested that Na^+ ion diffusion only occurs two dimensionally across the *ab* plane. Rapid capacity fading was observed in this material's electrochemical performance as its initial capacity of 110 mA h g^{-1} reduced to ~55 mA h g^{-1} by its 15th cycle.

4.3. Sodium metal phosphates and metal oxides

In section 3.2, a number of sodium metal phosphates were highlighted as potential alternative cathode materials to cobalt oxides. However, the diversity of their structural frameworks allows for the formation of stable sodium metal phosphates with various transition metals which may serve as anode materials. Recently, Yahia *et al*'s group [83] synthesised and tested different types of these materials as anodes for conventional NIBs.

Three phosphate-based materials were studied by this group; $NaCoCr_2(PO_4)_3$, $NaNiCr_2(PO_4)_3$, and $Na_2Ni_2Cr_2(PO_4)_3$, using NPD to solve their structures and propose Na vacancies. Refinement of the neutron diffraction data of the as-made materials revealed two Na vacancies in $NaCoCr_2(PO_4)_3$ and $NaNiCr_2(PO_4)_3$, and only one in $Na_2Ni_2Cr_2(PO_4)_3$. Charge–discharge curves also indicated two Na vacancies as the first discharge plateau capacities roughly corresponded to the intercalation of two Na^+ ions, for the former materials. However, a second plateau is also observed which likely corresponds to conversion reactions where the trivalent and divalent metal transition ions reduce to their metallic states, affording a capacity similar to the intercalation of 7 or 8 Na^+ ions. The cycling performances of the materials are unknown as the authors only presented electrochemical data for the first three cycles, hence their stabilities cannot be commented on [83].

The same group synthesised a similar material, $Na_2Co_2Fe(PO_4)_3$, and explored its electrochemical properties both as cathode and anode materials, individually [84]. Neutron diffraction data and bond valence sum calculations indicated an alluaudite-type structure with edge sharing $[MO_6]$ ($M =$ Fe, Co)

Figure 9. Structure parameters, *a* and *c*, calculated from NPD data as a function of Na^+ ion content, *x*, in $Na_x[Cr_{0.6}Ti_{0.4}]O_2$. Reproduced from [85]. CC BY 4.0.

chains linked together by the phosphate groups creating tunnels for Na^+ ions. The as-made material was tested as an anode (cycled between 0.03 and 3.00 V vs Na) and exhibited a capacity of $\sim$175 mA h g^{-1} at 10 mA g^{-1} in its second discharge after undergoing a conversion reaction in its first discharge that led to the collapse of the structure. To test the material as a cathode, it was first discharged to 0.9 V vs Na, allowing the intercalation of one Na^+ ion but preventing the conversion reaction from taking place. $Na_3Co_2Fe(PO_4)_3$ was then cycled between 1.8 and 4.5 V vs Na range and exhibited a capacity of $\sim$110 mA h g^{-1} at 5 mA g^{-1} rate in its second and third cycles. Again, the authors did not present further cycling data, therefore it is not possible to comment on the electrochemical stability of these materials.

Like sodium metal phosphates, sodium metal oxides have mainly been investigated as cathode-type materials for NIBs. However, in 2015, $Na_{0.6}[Cr_{0.6}Ti_{0.4}]O_2$ was explored as both a cathode and anode material in a symmetric Na-ion full-cell by Wang *et al* [85]. NPD analysis was used to reveal a brucite-type structure consisting of edge-sharing octahedral layers including transition metals with a trigonal prismatic interlayer space for Na^+ ions. The as-made material was initially tested as an anode and cathode material individually in half cells (exhibiting capacities of 120 mA h g^{-1} at 11.2 mA g^{-1} rate and 75 mA h g^{-1} at 7.6 mA g^{-1} rate, respectively) and then as both the positive and negative electrode in a full cell. The full cell gave a stable practical capacity of $\sim$70 mA h g^{-1} at 7.6 mA g^{-1} rate for 100 cycles with an operating voltage of $\sim$2.50 V vs Na. *In situ* XRD results indicated solid-solution behaviour during intercalation and deintercalation where phase transitions did not occur. The material was also synthesised with different amounts of Na and NPD patterns of these materials indicated that the *a* and *b* lattice parameters were shorter and the *c* lattice parameter longer for lower Na content (as depicted in figure 9). This indicated repulsion between the metal oxide groups as the Na^+ ions are no longer present to balance the repulsive force. Across a wide range of Na contents, the differences in these parameters were relatively small and therefore are not likely to be due to different phases of the material being formed. An absence of phase change suggests that the structure can accommodate a range of sodium contents, which may be the reason for the observed stable capacity.

Out of the anode materials studied, HCs show the most promising electrode material properties with high and stable practical capacities, typically around 300 mA h g^{-1}. *Ex situ* XRD and NMR studies have provided insight to the mechanisms behind the sloping and plateau voltage profiles. However, there are no published *ex situ* neutron studies of HCs post electrochemical cycling, to the best of our knowledge. Moreover, most of the of other anode materials for conventional NIBs indicate unfavourable phase transformations that hinder their cycling retention. Again, *ex situ* neutron diffraction at various states of discharge/charge could reveal the onset and origins of the phase transformations which can be taken into account when attempting to synthesise improved anode materials.

5. Application of neutron techniques on NIB electrolyte material investigation

5.1. Liquid electrolytes

To the best of our knowledge, there have been few studies of liquid electrolyte systems for NIB's using neutron scattering. This is perhaps due to the need for complex analysis procedures, and in most cases, the use of expensive deuterated solvents. However, careful analysis can reveal detailed and scientifically significant structures within the liquid.

Glymes are a class of short chain polyethene-oxides with general structure $CH_3–O(–CH_2–CH_2–O)_n–CH_3$. Diglyme ($n = 2$), has shown promise as a sodium electrolyte. In particular, diglyme allows sodium to intercalate into graphite as $Na^+(diglyme)_2$, which vastly increases the capacity

compared to carbonate solvents [86, 87]. Jensen *et al* [88] studied the solution structure of 1 M $NaPF_6$ in diglyme using neutron diffraction with isotopic substitution (NDIS); analysed using empirical potential structure refinement (EPSR). This method utilises the fact that different isotopes have different scattering lengths, but, to a first approximation, have the same underlying structure. In particular, hydrogen ($b = -3.74$ fm) can be exchanged for deuterium ($b = 6.67$ fm). This method has previously been successfully employed by Murphy *et al* [89] to study $LiNO_3$ and LiTFSI in tetraglyme. In the study of $NaPF_6$ in diglyme, six difference isotopic variants of diglyme were measured. These data were analysed by the EPSR method, where an atomistic Monte Carlo simulation of the system is refined against the data by use of an additional, empirical, potential. The resulting three-dimensional ensemble is the best fit to the data and can then be analysed to obtain a wealth of structural information. The study showed that 83% of Na^+ exists as $Na^+(diglyme)_2$ in the liquid state suggesting the solution structure may be important for intercalation.

5.2. Solid electrolytes

5.2.1. Sodium β-aluminas

The first QENS study of Na^+ dynamics in a SSE material was on polycrystalline Na β-alumina ($Na_{1.25}Al_{11}O_{17.125}$) [90]. Its structure consists of densely packed spinel blocks of oxygen and aluminium atoms separated by mirror planes containing mobile Na^+ ions. In 1937, anomalies were found in the structure where Na^+ ions were present and these sites were subsequently named after their discoverers; Beevers and Ross [91]. XRD and NPD studies revealed that cations occupied three possible sites in the conducting mirror plane within the unit cell; one Beevers and Ross site (BR), one anti-Beevers and Ross site (aBR) and three middle oxygen sites (mO, between two O spinel bonding atoms), as shown in figure 10. Singly occupied cells with a single Na^+ ion at a BR site is predicted to be 'fixed' with only oscillations around the site, thus no jumps would be executed and detected on the experimental time scale. Multi-occupancy of planes must therefore be achieved with cation pairs lying in mO sites and with triangular clusters of three cations, Na_3 (mO_1, mO_2, mO_3), with each arrangement having different cation dynamics.

Two kinds of motions were characterised by QENS; with thermally activated localised local jumps $\leqslant 25\,°C$ and long range liquid-like diffusion $\geqslant 125\,°C$ with lower probability and longer correlation time than the local jump. For observed motion at $\leqslant 25\,°C$, cations in multi-occupied cells were considered to execute localised jumps among the possibility of two, three, four and seven positions in the unit cell. Good fits to the experimental data were obtained when considering jumps among three positions (mO_1-BR-mO_2 or aBR-mO-BR) or four positions (back and forth between three equivalent mO and stable BR or aBR). These localised jumps of $E_a \approx 50$ meV between mO sites with residence time of 1.2×10^{-11} s are the dominant processes up to 300 °C and the fraction of mobile species involved in these local motions at 300 °C is about 0.13. The residence time of cations in mO sites is reduced by a factor of two at 400 °C, due to destabilisation. This increases the fraction of mobile species from 0.13 to 0.2 for 25 °C–125 °C, ascribed to the reduction in size of the domains involved in the long range diffusion process. The long range diffusion process has a diffusion coefficient $\sim 7.5 \times 10^{-6}$ cm^2 s^{-1} derived from a liquid-like model with an $E_a \approx 130$ meV to remove defects blocking the conduction paths. The activation energy for long range conduction was found to be the sum of the local barrier and of defect annihilation; $50 + 130$ meV.

Building on the previous experiment, a single Na β-alumina crystal was used in an orientation that resulted in the majority of inelastically scattered neutrons. This is associated with in-plane Na^+ displacements that can be used to characterise the diffusion model where local and extended motions are considered simultaneously [92]. This work corroborated the previous analysis at 300 °C, 18% of ions corresponding to doubly occupied cells underwent 'localised' motions restricted to a given cell with a residence time of $\sim 3 \times 10^{-11}$ s. At 400 °C, temporary multi-occupancy of ions moving through adjacent cells increase the quantity of ions (63%) able to undergo long-range motions on a time scale of $\sim 1.5 \times 10^{-10}$ s. O_1 interstitial oxygen atoms are described as the blocking defects which make the conduction mostly one dimensional along segments of about seven cells via the caterpillar mechanism with $E_a \approx 80$ meV.

5.2.2. Sodium metal phosphates and silicates

As discussed in section 3.2, when NIB technology was at its infancy, sodium metal phosphates were considered principally as alternative cathode materials to sodium metal oxides. Since an interest in all-solid-state NIBs has emerged, these materials are now being considered as SSEs for their high ionic conductivities.

A nitridophosphate, $Na_3TiP_3O_9N$, was studied by Liu *et al* [93] mainly as a NIB cathode material but its isotropic ion conduction property also makes this material a prospective solid electrolyte. A NPD study revealed its three distinct Na^+ ion site vacancies and bond valence sum calculations indicated that sites Na(1) and Na(3) have the weakest bonding to the surrounding oxygen atoms. This was confirmed when NPD of the chemically desodiated material indicated depopulation of the Na(1) site. Furthermore, TOF NPD at higher
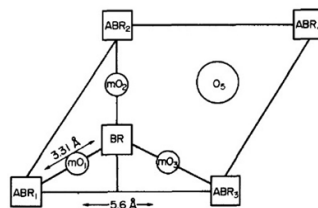
Figure 10. Diagram showing the available sites for Na$^+$ ions in Na$_{1.25}$Al$_{11}$O$_{17.125}$ where BR, aBR and mO represent Beevers and Ross, anti-Beevers and Ross, and middle oxygen sites (at a mid-distance between two oxygen atoms), respectively. Reprinted from [90], Copyright (1987), with permission from Elsevier.

temperatures showed enhancement of Na(1) and Na(3). These findings give insights to the type of mechanism behind ionic diffusion within the material.

Famprikis *et al* [94] discovered a third, new phase of a thiophosphate, Na$_3$PS$_4$, by heating the material to 545 °C. Both synchrotron XRD and neutron diffraction experiments were used to characterise this new phase as diffraction peaks associated with other phases disappeared and new peaks emerged. DFT showed a high level of disorder of Na$^+$ ions in the new phase and MD was used to indicate higher diffusion coefficients with respect to the other phases. Additionally, MD demonstrated translational movement of the Na$^+$ ions while PS$_4^{3-}$ anions exhibited rotational motion and remained translationally fixed about their positions. These results indicate promising qualities for a SSE, but a stable form of this new phase would be required at a lower temperature for its potential application in all-solid-state NIBs.

NASICON materials, first reported in 1976 by Goodenough and Hong for high temperature NIBs [95], are now being revisited for all-solid-state NIBs. NASICONs generally contain 3D networks of ZrO$_6$ octahedra and PO$_4$ or SiO$_4$ tetrahedra where Na$^+$ ions can move along three dimensions. These materials have exceptional ionic conductivities, on the order of 10^{-3} S cm^{-1} [96, 97], matching that of some conventional organic liquid electrolytes [98]. Depending on their synthesis and stoichiometry, NASICON materials can exist in different phases and exhibit a range of ionic conductivities.

Since Goodenough and Hong's first report of Na$_{1+x}$Zr$_2$Si$_x$PO$_{12}$ (where $0 < x < 3$) which revealed two Na vacancies in the as-made material [95], other papers have suggested that the actual number of Na site vacancies is higher, with some finding three [99–101] and recently, Zhang *et al* reporting five [102]. In these cases, TOF NPD was employed to extract the occupancies of the various sites by considering the integrated areas of the associated peaks. Many of the older papers reporting two Na sites proposed ionic conduction occurring via Na(1)–Na(2) or Na(2)–Na(2) as Na(2) was found to have higher occupancies [95, 103]. On the other hand, the recent study revealing five Na sites indicated that the ionic conductivity arises from several Na$^+$ ions simultaneously jumping to their adjacent sites (via correlated migration) as opposed to individual Na$^+$ ions hopping between sites. AIMD simulations were used to propose this type of mechanism. The simulations were performed at high temperatures to drive the diffusion of Na$^+$ ions and visualise their preferred migration pathways. By extracting the ratio of correlated jumps over all jumps from the MD simulations, results also showed that the number of these correlated jumps increases with temperature, and with the concentration of Na$^+$ ions (presented in figure 11). This theory was supported experimentally by the increase in ionic conductivity through alternating current impedance spectroscopy. The positive correlation between ionic conductivity and concentration of Na$^+$ ions was also found for many of other the studies. The general consensus for explaining this trend was that the increase in Coulombic repulsions (with the increasing amount of Na$^+$ ions) lowered the energy barriers for other Na sites, since repulsion forced Na$^+$ ions into the previously higher energy sites [95, 99–101, 103]. Deng *et al* [104] attempted to substitute some of the Zr^{4+} cations with Sc^{3+} cations in the hope to increase the material's electrochemical stability window since Sc^{3+} is redox inactive. However, this substitution reduced its ionic conductivity and increased the activation energy for ion diffusion. Moreover, increasing the amount of Sc^{3+} reduced the atomic displacement parameters, implying a reduction in Na$^+$ ion mobility.

Scandium-based NASICON structures have since been revisited without zirconium. Guin *et al* [105] synthesised Na$_{3.4}$Sc$_2$Si$_{0.4}$P$_{2.6}$O$_{12}$ through a solid state reaction and found that it actually contained two phases; monoclinic and rhombohedral phases of equal amounts, through refinement of XRD and NPD data. Although their lattice parameters were very similar, Si was only present in the rhombohedral phase. Additionally, the two-phase sample was found to exhibit higher ionic conductivity (3.5×10^{-4} S cm^{-1}) than that of its individual components. The authors predict that there is an increase in the number of favourable hopping distances for Na in the two-phase sample which could explain the synergistic effect on its ionic conductivity, compared to the individual phases. Recently, Santhoshkumar *et al* [106] compared a similar
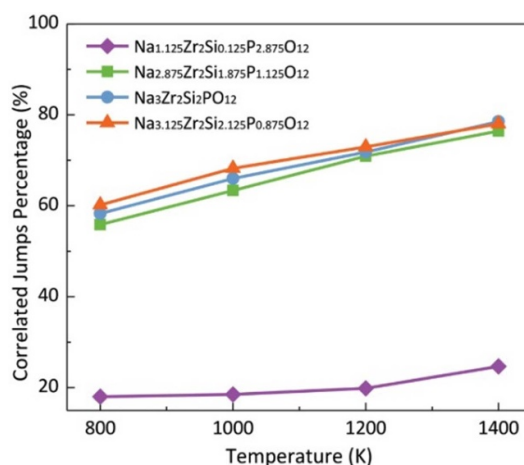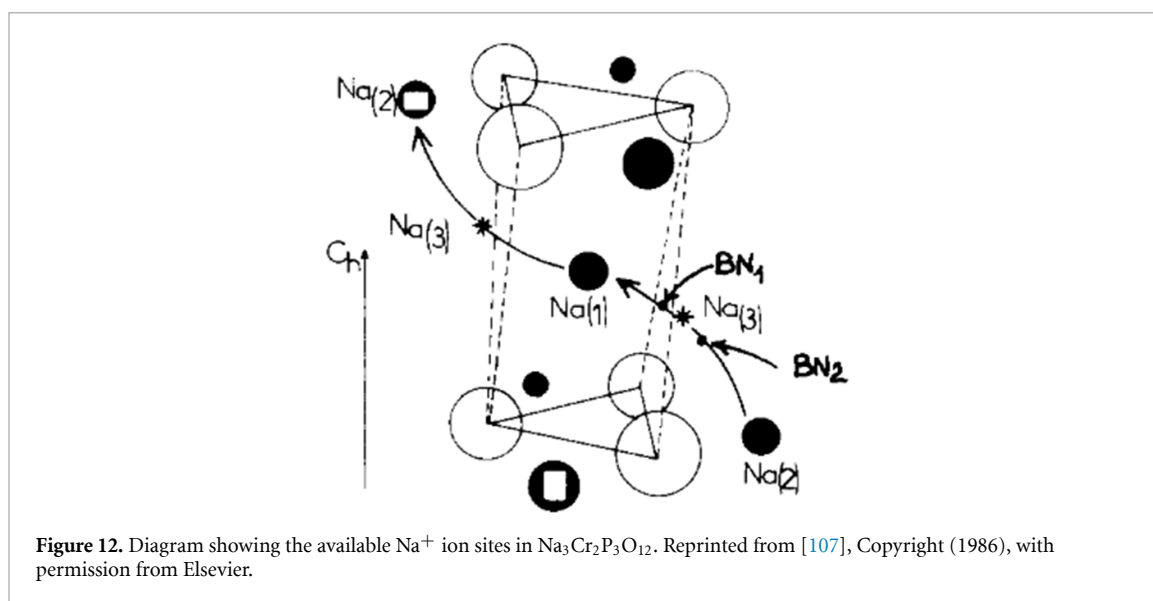
Figure 11. The change in the percentage of correlated jumps, calculated by AIMD, with temperature, and with the concentration of Na^+ ions in the materials. [102] John Wiley & Sons. [Copyright © 2019 WILEY-VCH Verlag GmbH & Co. KGaA, Weinheim].

material with different amounts of Si; $Na_{3+x}Sc_2Si_xP_{3-x}O_{12}$ where $x = 0.0, 0.2, 0.4$ and 0.8. Again, XRD and NPD were used to identify the structure types of each material, which were found to be monoclinic for the sample without Si and rhombohedral in all other cases. The highest ionic conductivity was observed when $x = 0.4$ (2.4×10^{-3} S cm^{-1}) through alternating current impedance spectroscopy. When $x = 0.8$, a much lower ionic conductivity of 4×10^{-6} S cm^{-1} was observed. The ratio of vacant to occupied Na sites may explain this behaviour since this ratio is the smallest for $x = 8$. However, this ratio is largest for $x = 2$ and yet it does not exhibit the highest ionic conductivity. The poor ionic conductivity for when $x = 0.8$ more likely stems from its larger grain size which was observed in its SEM and therefore suggests a larger grain boundary resistance.

A combination of NPD and QENS was used by Lucazaeu *et al* [107] to study $Na_3Cr_2P_3O_{12}$. The sodium ions are distributed among three main sites, Na(2) are octahedrally distributed around Na(1) sites, with metastable Na(3) (less occupied at higher temperatures) positioned between both 'bottlenecks' BN_1 and BN_2 (shown in figure 12). An ionic conductivity 500 times greater than $Na_3Zr_2P_3O_{12}$, which only has Na(1) site occupation, suggests partial filling of Na(2) sites to be required for reasonable Na mobility. From this structural understanding, the diffusion path of a Na^+ ion sitting in a Na(1) site was predicted to proceed in a straight line via a vacant Na(2) site, to metastable BN_1 (in the middle of the $O_1O_2O_3$ triangle), then passing at the Na(3) position and again through BN_2. Whilst $Na_3Cr_2P_3O_{12}$ has a strongly **Q**-dependent HWHM and intensity at 400 °C, no quasi-elastic signal was observed for $Na_3ZrMgP_3O_{12}$ and $NaZr_2P_3O_{12}$, agreeing with their lower ion conductivity. At 400 °C the model of Na^+ ion jumps between Na(1) and Na(2) sites ($d = 3.5$ Å) revealed a corresponding residence time in Na(1) $\approx 4 \times 10^{-12}$ s and occupation factor ≈ 0.75. At 150 °C the jump distance was found to decrease towards 1.5 Å, and was predicted to be due to the added involvement of the Na(3) site in the jump mechanism.

α-Na_3PO_4 is both a plastic phase and a good sodium ion conductor ($10 \, \Omega^{-1}$ cm^{-1} at 325 °C) [86]. The way in which the transport of cations is enhanced by a dynamic coupling to the reorientational motion of the translationally fixed polyatomic anions was explored by QENS of oxygen coherent scattering with energy resolution of 100 μeV and 270–360 μeV. High-resolution spectra consisted of two contributions: incoherent elastic scattering from sodium (but quasi-elastic hopping motion was too slow to be distinguished from the elastic scattering) and **Q**-independent quasi-elastic coherent oxygen scattering, reflecting the localised character of phosphate anion reorientation. The reorientational mode of tetrahedral anion motion was fit to various mechanisms and fit best when three mobile ions were modelled to undergo continuous or jump rotational diffusion (1.47 Å) about a fixed C_3 axis in a cubic environment. This agrees with x-ray structural investigation that observed one of the P–O bonds preferentially oriented along d_{111}, while the scattering density of the remaining three oxygen atoms was smeared out. The reorientational dynamics were described with a single time constant which is thermally activated with $E_a \approx 184$ meV. Additional quasi-elastic intensity at $0 < Q < 1.5$ Å^{-1} suggested the involvement of sodium ions further away from the centre of rotation in the reorientational motion of some of the anions.

Gupta *et al* [87] compared the diffusion of Na^+ ions in the amorphous phase of $Na_2Si_2O_5$ with its crystalline orthorhombic phase. The amorphous phase was found to have different medium range

Figure 12. Diagram showing the available Na^+ ion sites in $Na_3Cr_2P_3O_{12}$. Reprinted from [107], Copyright (1986), with permission from Elsevier.

orientations of silicon polyhedral units that were not available in crystalline orthorhombic phase, opening up several accessible pathways. *Ab initio* simulations show preferential Na diffusion within layered channels by corner shared SiO_4 tetrahedra in the amorphous sample. A HR jump-diffusion model, fit to QENS at 475 °C corroborated with MD simulation at 725 °C, gave a mean jump length of 2.6–3 Å, residence time of 9–15.4 ps, and a diffusion coefficient of $1.6 \pm 1.1 \times 10^{-10}$ m^2 s^{-1}, matching well with first neighbour distance of 2.98 Å in the amorphous phase. The authors noted discrepancies in the results to be due to the inherent short comings of the various techniques, with MD simulations using a cell of finites size and poor QENS statistics for observation of slow Na^+ dynamics.

Most of the studies involving NPD and QENS of NASICON materials are from the 1970s and 80s [95, 99–101, 103], back when NASICONs were proposed as solid electrolytes for high temperature NIBs consisting of liquid sodium electrodes. This research may now be considered outdated and newer neutron studies of current all-solid-state NIB electrolytes will be required to understand the causes behind such conductivities for these batteries.

5.2.3. Sodium metal sulphides
Sulphide-based compounds have been of particular interest as SSEs due to their remarkable ionic conductivities. However, most of these materials are not air-stable and can form toxic hydrogen sulphide gas under ambient conditions. In recent years, researchers have attempted to synthesise air-stable versions of sodium metal sulphides with competitive ionic conductivities.

The sulphide-based electrolyte, sodium thioantimonate (Na_3SbS_4) is a promising SSE that exhibits impressive room temperature chemical stability and ionic conductivity (1–3 mS cm^{-1}). Neutron diffraction of the room temperature tetragonal crystal structure revealed two main sites for Na atoms in the Na_3SbS_4 lattice; Na(1) in a NaS_6 distorted octahedron, and Na(2) in a NaS_8 dodecahedron [108]. In the *x, y*-plane, the NaS_6 and NaS_8 sites are alternately connected by shared faces to form an infinite planar tunnel network, –Na(1)–Na(2)–Na(1)–Na(2)–, with a 5% vacancy of the Na(2) site within the tunnel, revealed by Rietveld refinement. NaS_6 octahedra were also found to be mutually linked with shared edges along the *z*-axis, allowing Na^+ ions to hop across the planar network. This suggests a 3D tunnel network of intra- and inter-planar chain pathways which gives rise to the rapid Na^+ ion transport.

It was recently shown that Na_3SbS_4 experiences a reversible phase transition from a tetragonal phase at room temperature to a cubic phase at elevated temperatures (>160 °C) [109]. This transition results in not only a minimal conductivity increase due to similar lattice parameters and volume, but also a reduced activation energy for the diffusion process. DFT revealed a lower diffusion barrier of 120 meV for 3D migration of Na^+ through a cubic vs tetragonal structure in the *x, y*-plane (650 meV) and *z*-plane (450 meV) due to differences in interatomic Na–S/Sb distances and repulsion energies. The EFWS showed initiation of a diffusive process at 0 °C, whilst a Gaussian approximation showed a distinct transition between two temperature dependent regions of average MSD due to crystalline structures. A fit of the Q dependent QENS signal to the CE model showed the jump length to become much shorter (4.83–2.86 Å), whilst the residence

time decreased (from 310.1 to 65.6 ps) when increasing from 100 °C to 250 °C (tetragonal to cubic). This change in dynamics corresponded to different site hopping; Na^+ ion hopping from Na(1) to Na(2) site in tetragonal, and Na(1) to Na(1) in cubic Na_3SbS_4.

5.3. Sodium borohydrides

The previous investigations have used QENS to study the mechanisms occurring within already known superionic conducting material SSEs. However, QENS has the potential to support material discovery, and has been used extensively by the group of Udovic *et al* [110–114], to obtain a comprehensive understanding of the mechanisms occurring in a range of polyanion borohydride salts.

Based on the parent compound tetrahydroborate (BH_4^-), larger $B_{12}H_{12}^{2-}$ polyanions were found to undergo entropy driven order–disorder phase transitions at lower transition temperatures providing fast-ion conduction (0.1 S cm^{-1} > 205 °C) [115]. This was predicted to be due to the lattice stacking of large translationally immobile, highly reorientationally mobile, and chemically inert (~7 Å diameter) anions affording spacious interstitial channels with a surplus of favourable cation sites compared to cation numbers for efficient conduction. QENS studies have revealed the underlying mechanism of Na^+ ion conduction in these polyanion structures guiding chemical modifications that have provided a new class of superionic conductors as potential SSEs.

NPD of $Na_2B_{10}H_{10}$ [115] revealed Na^+ ions partially occupying a variety of interstitial sites within the orientationally disordered lattice of $B_{10}H_{10}^{2-}$ anions above ~85 °C, much reducing the temperature required for phase transition in $Na_2B_{12}H_{12}$. EFWS revealed an order of magnitude increase in reorientational mobility upon disordered phase formation, and QENS at 100 °C suggested the reorientational jumps to occur both around the long axis and as two-fold flips of apical H atoms with a jump correlation frequency $\sim 3 \times 10^{10}$ s^{-1}. ^{23}Na NMR confirmed a highly mobile long range cation sub-lattice within the less restrictive interstitial pathways formed by the large anions providing $\sigma \approx 0.01$ S cm^{-1} at 110 °C. An order of magnitude higher anion jump rate compared to cation jump rate may provide a cooperative environment inducing the lowered cation diffusion barrier. This finding motivated future design of increasing Na^+ diffusion by increasing anion rotational mobility.

A 1:1 cation : anion ratio in monovalent $NaCB_{11}H_{12}$ was predicted to reduce the columbic attractions between mobile anions and cations [114]. Additionally, doubling the number of cation vacancies was speculated to increase orientational mobility and thus enhanced cation diffusion. Neutron vibrational spectra and simulated PDOS from DFT corroborate a disordered crystal structure for $NaCB_{11}H_{12}$ above the phase transition. The lattice constant at 90 °C was over 2% larger than in $Na_2B_{10}H_{10}$ at 135 °C providing more space for cation transport. $NaCB_{11}H_{12}$ also exhibited a conductivity of 0.12 S cm^{-1} at 110 °C with $E_a = 220$ meV. The quasi-elastic signal for $Q > 1$ Å^{-1} confirmed the presence of the same small angle jump reorientations from both one axis to multi axis reorientations as the previous $Na_2B_{10}H_{10}$. Computational chemical calculations to estimate partial atomic charges based on Mulliken population analysis of atomic orbitals confirmed the effect of atomic positioning on the rotational dynamics. A combination of the increased free space and fivefold greater positive Mulliken charge on H(–C) than H(–B) led to a preferred vertex position of C atoms that resulted in a (60%) greater reorientational mobility of $CB_{11}H_{12}^-$.

The spatial and temporal mechanisms behind cooperative anion-cation mobility in $NaCB_{11}H_{12}$ were further investigated with AIMD and QENS [113]. Cations appeared to locate at threefold coordinated boron faces, particularly at the icosahedron farthest from the carbon axis, due to a strong repulsive interaction between cations and anions with an energy difference of ~1 eV between the C or B faces. QENS obtained one narrow and one wide Lorentzian function, associated with anion reorientational jumps and low frequency overdamped anion vibrational modes, respectively. Q dependence of relative elastic and inelastic intensity suggested a small-angle reorientational jump mechanism (correlation frequency $>3 \times 10^{10}$ s^{-1}), in the form of five-fold jumps about the C_5 axis, plus small canting angles from 10° to 20°. This was corroborated by faster B atom dynamics than C atoms in the AIMD at 225 °C. Carbon addition was confirmed to modify the orientational preference of the anions and aid rotational mobility, creating additional symmetry incompatibilities that inhibit ordering to lower temperatures and provide anions ten and three times more mobile than $B_{12}H_{12}^{2-}$ at 90 °C and 205 °C, respectively.

The smaller cluster, $NaCB_9H_{10}$ was later studied [111] and found to exhibit a transition at 25 °C to form disordered hexagonal symmetry with liquid like conduction of 0.03 S cm^{-1}. QENS revealed two distinct reorientational jump rates of 8×10^{11} s^{-1} and 6×10^{10} s^{-1}, both orders of magnitude higher than cation diffusion jump rates obtained through NMR. These were assigned to small angular jumps around the anion C_4 symmetry axis and 180° flips perpendicular to this axis. The C_4 axis rotation jump was found to occur faster than in the $Na_2B_{10}H_{10}$ analogue. This observation was rationalised by the anomalously higher positive Mulliken charge on the apical H(–C) that would influence anion reorientations. Moreover, all the $CB_9H_{10}^-$ H atoms have a positive charge (unlike negative $B_{10}H_{10}^-$ H atoms) and thus provide less stable cation sites

with reduced hopping activation energy. These factors contribute to an increased cooperative nature of anion reorientation enabling facile cation transport and therefore provide $NaCB_9H_{10}$ with the most impressive ionic conductivitiesobserved yet amongst complex-hydride-based materials.

Mixing of the individual cluster types is another route investigated to improve the performance of these materials, which leads to non-additive improvements to ion conduction. Specifically, an ionic conductivity of 0.9 mS cm^{-1} was reached at 20 °C for $Na_2(B_{12}H_{12})_{0.5}(B_{10}H_{10})_{0.5}$ [116]. Temperature dependent conductivity was found to pass through three different regimes with differing activation energies. The specific regime dynamics were probed by correlating QENS, impedance, and NMR spectroscopy. Conductivity remained low below −50 °C until the glass transition, where faster diffusion occurred with $E_a \approx 600$ meV. Correlated ion diffusion originates from the coupling of the cation and anion motions due to short range ion-ion interactions combined with background energy fluctuations associated to fast anion vibrations. QENS showed the involvement of specific symmetry axis anion rotations that suggested this correlation to be a cation-anion docking-undocking diffusion mechanism, with each anion being able to initiate jumps to multiple Na$^+$ ions due to their respective size. Above 70 °C, Na$^+$ ion disordering within the sublattice and non-correlated ion diffusion caused the E_a to decrease to 340 meV. QENS revealed anion rotations to be enhanced compared to the pristine materials and ^{11}B NMR showed that $B_{12}H_{12}$ rotations entered the NMR timescale at lower temperature than $B_{10}H_{10}^-$, in contrast to the observations of the pure compounds. This confirms that interaction between the two anion types causes the enhanced dynamics and thus ionic conductivity, but requires further investigation, such as QENS with ^{11}B enriched samples.

6. *In situ* and *operando* neutron scattering

Ex situ battery studies often provide useful insights and allow researchers to make logical predictions regarding electrodes under operation. However, *ex situ* experiments require dismantling the cell after cycling and preparing the electrode for characterisation. This method may compromise the components through washing, and possible exposure to ambient atmosphere when transferring samples to the instrument. In contrast, *in situ* and *operando* experiments capture information about the components as assembled in a battery environment. The two terms are often used interchangeably in literature which is not always accurate. *In situ* usually refers to the analysis of a specific area within a battery environment while *operando* refers to the analysis during battery operation such as cycling. By these definitions in battery research, all *operando* studies are *in situ*, yet all *in situ* studies cannot be classed as *operando* [33, 118].

In situ studies can also exploit the tuneable sampling environment of some neutron instruments, for example, the capability to investigate how battery materials change with varying temperature or pressure. Zhu *et al* [120] tracked the lattice changes of antiperovskites, Na_3OBr and Na_4OI_2, with temperature using sealed quartz capillaries and TOF powder neutron diffractometer NOMAD (Nanoscale-Ordered Materials Diffractometer) at SNS (Spallation Neutron Source), Oak Ridge National Laboratory [120]. Neutrons were chosen for this experiment to obtain more accurate positions of the oxygen atoms than would be achievable with x-rays. From the neutron data, lattice parameters, thermal expansion coefficients, and defect occupancies were derived.

The highly penetrating and non-destructive nature of neutrons has led to characterisation of Na-ion full cells, for example cylindrical 18 650s. Chen *et al* [117] measured neutron diffraction of an 18 650 cell during a charge step to supplement an investigation of Na$^+$ insertion and extraction from P2-$Na_{2/3}[Fe_{1/3}Mn_{2/3}]O_2$ cathode. By tracking the changes in the d_{200} and d_{102} lattice spacings, the local and crystal distortion could be detected with voltage and Na$^+$ ion deintercalation (figure 13). *Operando* studies such as this by Chen *et al* characterise the chemical or physical changes in batteries whilst they undergo charge or discharge. In another experiment, *operando* NPD of a 25-layer pouch cell was combined with first principles to study $Na_{0.5}Ni_{0.25}Mn_{0.75}O_2$ cathode, as shown in figure 14 [119]. The evolution of high voltage phases was shown to proceed as P3 to O3 from above approximately 3.7 V and O3 to O3s when the voltage exceeded around 4.0 V. In the pristine P3-type $Na_{0.5}Ni_{0.25}Mn_{0.75}O_2$ synthesised at 650 °C, local Ni–Mn ordering due to large valence difference was detectable by NPD through the observation of two extra asymmetrically broadened peaks. These are not observed in XRD of the same material because Ni and Mn have similar atomic numbers and therefore have weak contrast in x-ray scattering. In the *operando* NPD data in figure 14, peaks from the 006 reflections of the cathode, as well as peaks from the HC anode and the polyvinyl difluoride separator were observed below $2\theta = 52°$.

Standard cell designs (cylindrical, pouch, or coin) have been adapted using casements made of materials that have minimal Bragg scattering, such as Ti–Zr alloys (null-matrix) or vanadium, to make custom cells for *operando* neutron studies of LIBs. For a comparison of cell types and geometries adapted to various scattering instruments, we direct the reader to the recent review by Liang *et al* [121]. Zhao *et al* [31] includes experimental set-ups for other neutron techniques including reflectometry, and neutron imaging, in the
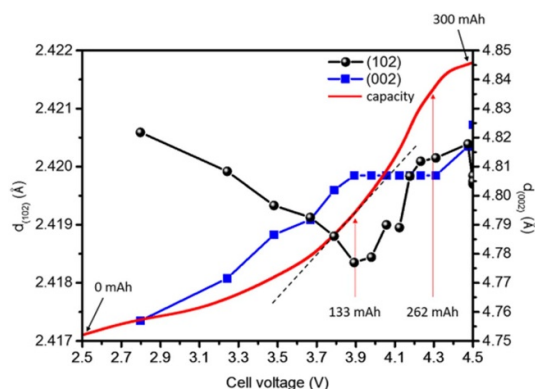
Figure 13. Changes in the d_{200} and d_{102} lattice parameters of P2-$Na_{2/3}[Fe_{1/3}Mn_{2/3}]O_2$ cathode of an 18 650 cell operating between 2.5 and 4.5 V. Reprinted with permission from [117]. Copyright (2018) American Chemical Society.
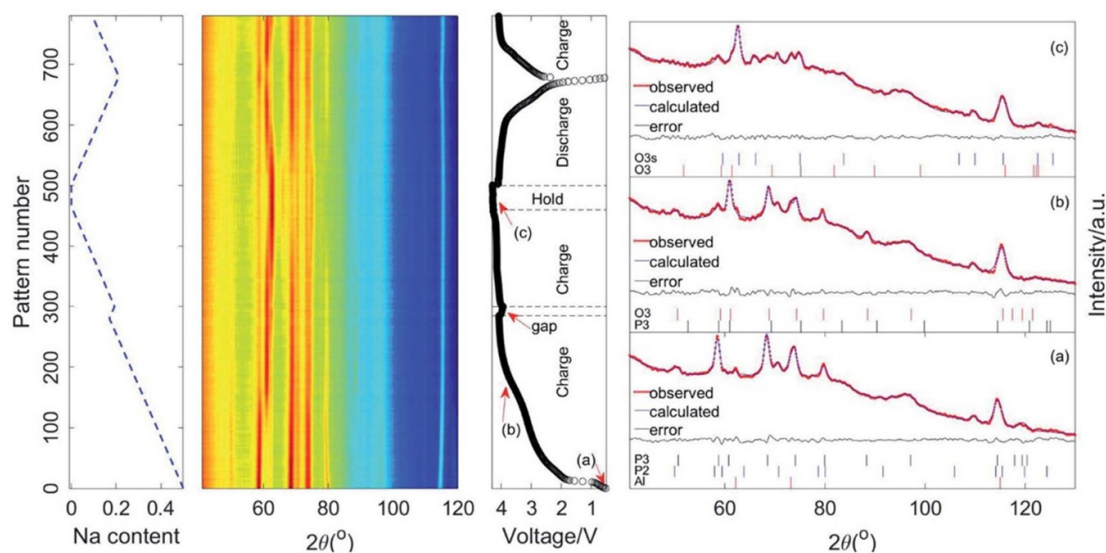

Figure 14. NPD of the $Na_{0.5}Ni_{0.25}Mn_{0.75}O_2$-HC pouch cell connected while cycling at 10 mA g^{-1} rate. Reproduced from [119] with permission of The Royal Society of Chemistry.

in-situ section of their review. Although, to our knowledge, the custom cells presented to date for *operando* battery studies have not yet been applied to NIB chemistries, this could easily be achieved by substituting NIB materials to use these cells for *operando* studies of NIBs. We have found only two cases where *operando* characterisation is employed for NIB cells, both of which use commercial cell designs [117, 119].

Challenges to *operando* studies on standard cell designs such as 18 650s, and custom cylindrical-type or pouch-type cells arise from the presence of multiple components, which are often arranged in several repeating layers. Each atom present in a sample will interact with incident neutrons in one of three ways: coherent scattering, incoherent scattering, and absorption. Furthermore, even in elastic scattering experiments, inelastic scattering events will occur, and also some isotopes (e.g. protons) will give a high incoherent background. This has impacts on the signal detected and the subsequent data processing. Therefore, in cells with multiple cathode, anode, and separator layers, it is easier to track structural changes of crystalline cathodes and anodes that give rise to distinct Bragg peaks, as opposed to components with greater disorder, such as HC anodes.

To study disordered materials like HC, experimental design should focus on maximising the signal of the material under interrogation relative to the background noise and other components present. Custom cell designs such as that in figure 15(a) designed for the VULCAN diffractometer at Oak Ridge National Laboratory use a large electrode area (60 mm^2) to maximise the volume of material in the beam and a single layer of anode, separator, and cathode to minimise the other components in the neutron beam [122]. Using similar design principles, we have designed a custom-built cell for neutron scattering for the NIMROD
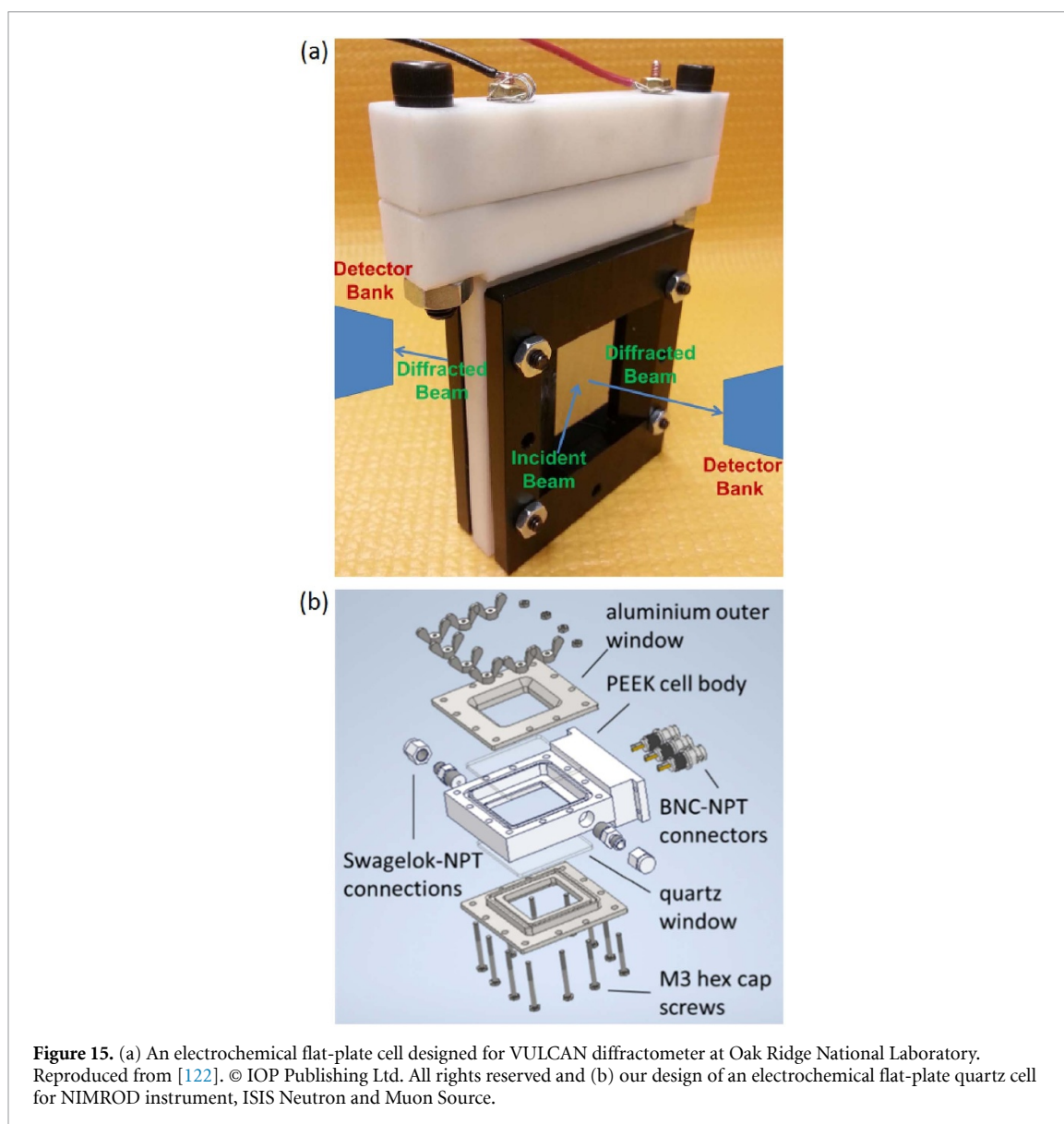
Figure 15. (a) An electrochemical flat-plate cell designed for VULCAN diffractometer at Oak Ridge National Laboratory. Reproduced from [122]. © IOP Publishing Ltd. All rights reserved and (b) our design of an electrochemical flat-plate quartz cell for NIMROD instrument, ISIS Neutron and Muon Source.

instrument at ISIS, UK, (figure 15(b)) which benefits from probing a wide range of correlated length scales, and allows for electrode areas of up to 900 mm^2.

The cell is designed with quartz glass windows which have no Bragg peaks or contributions to small angle scattering. Three BNC-NPT connections in the top of the cell allow for 2-electrode or 3-electrode electrochemistry. Two additional holes drilled into the sides of the PEEK cell body and fitted with PTFE Swagelok-NPT connections provide both an inlet and outlet for electrolyte fill. A robotic stage to move the cell into different areas of interest from the cabin has been developed. With careful consideration of how the components are configured within the cell, the robotic stage could allow the cathode, anode, and electrolyte, to be probed individually in *operando* experiments. When used with the NIMROD instrument this will allow simultaneous *in situ* measurement of changes in pore filling (from SANS), the local atomistic structure of the electrodes (from diffraction and PDF) and potentially the structure of the electrolyte from NDIS and EPSR.

7. Conclusions

To summarise, we have reviewed neutron diffraction studies of as-made cathode and anode materials for conventional NIBs, and solid electrolytes for all-solid-state NIBs. We have also highlighted the lack of *ex situ* experiments of these materials post electrochemical cycling. Very few NIB cathode materials were analysed by neutron diffraction after exposure to electrochemical conditions and no anode or solid electrolyte materials were studied in this way, to the best of our knowledge.

Neutron diffraction characterisation has proven to be an effective analytical technique for the elucidation of various structural phases, Na site vacancies (and their occupancies), and the possible pathways taken by Na^+ ions during cycling are inferred. This technique most often exceeds the limitations of XRD when it comes to investigating the movement of small elements like sodium and distinguishing between transition metal cations with similar atomic numbers such as the ones used in cathode materials for NIBs.

It was also shown that QENS studies of cathode and SSE materials have provided useful insight into the diffusion of Na^+ ions within these materials. Material phase changes at various temperatures observed in NPD and XRD patterns are complemented by QENS characterisation. Moreover, this technique can also lead to new material discovery, such as in the case of polyanion sodium borohydride salts as potential SSEs.

Although conventional NIBs are a more economically viable option and all-solid-state batteries are a safer option compared to commercial LIBs, they are still far from meeting the high practical capacities and cycle lives that LIBs offer. Therefore, *ex situ*, possible *in situ*, and *operando* neutron scattering studies are critical in determining the exact causes of the instability and such low capacities of electrode materials for NIBs. These studies will reveal the parts of the materials that hinder their electrochemical performance and will therefore help direct syntheses of different phases or new materials in future research.

Data availability statement

No new data were created or analysed in this study.

Acknowledgments

ORCID iDs

Ami R Shah ● https://orcid.org/0000-0002-4584-937X
Rebecca R C Shutt ● https://orcid.org/0000-0001-8092-6409
Jennifer Hack ● https://orcid.org/0000-0002-5529-4750

References

[1] Stimming U 2020 Current state and future prospects for electrochemical energy storage and conversion systems *Energies* **13** 5847
[2] Yoshino A, Sanechika K and Nakajima T 1987 Secondary Battery 4,668,595
[3] Liu C, Neale Z G and Cao G 2016 Understanding electrochemical potentials of cathode materials in rechargeable batteries *Mater. Today* **19** 109–23
[4] He Y, Ren X, Xu Y, Engelhard M H, Li X, Xiao J, Liu J, Zhang J-G, Xu W and Wang C 2019 Origin of lithium whisker formation and growth under stress *Nat. Nanotechnol.* **14** 1042–7
[5] Besenhard J O and Eichinger G 1976 High energy density lithium cells. Part I. Electrolytes and anodes *J. Electroanal. Chem.* **68** 1–18
[6] Greim P, Solomon A A and Breyer C 2020 Assessment of lithium criticality in the global energy transition and addressing policy gaps in transportation *Nat. Commun.* **11** 1–11
[7] Rüdorff W 1959 Einlagerungsverbindungen mit Alkali- und Erdalkalimetallen *Angew. Chem.* **71** 487–91
[8] Weaving J S *et al* 2020 Elucidating the sodiation mechanism in hard carbon by operando Raman spectroscopy *ACS Appl. Energy Mater.* **3** 7474–84
[9] Moriwake H, Kuwabara A, Fisher C A J and Ikuhara Y 2017 Why is sodium-intercalated graphite unstable? *RSC Adv.* **7** 36550–4
[10] Nobuhara K, Nakayama H, Nose M, Nakanishi S and Iba H 2013 First-principles study of alkali metal-graphite intercalation compounds *J. Power Sources* **243** 585–7
[11] Stevens D A and Dahn J R 2000 High capacity anode materials for rechargeable sodium-ion batteries *J. Electrochem. Soc.* **147** 1271
[12] Stevens D A and Dahn J R 2001 The mechanisms of lithium and sodium insertion in carbon materials *J. Electrochem. Soc.* **148** A803
[13] Crabtree G, Kócs E and Trahey L 2015 The energy-storage frontier: lithium-ion batteries and beyond *MRS Bull.* **40** 1067–76
[14] Dahn J R, Xing W and Gao Y 1997 The 'falling cards model' for the structure microporous carbons *Carbon* **35** 825–30
[15] Au H *et al* 2020 A revised mechanistic model for sodium insertion in hard carbons *Energy Environ. Sci.* **13** 3469–79
[16] Stevens D A and Dahn J R 2000 An *in situ* small-angle x-ray scattering study of sodium insertion into a nanoporous carbon anode material within an operating electrochemical cell *J. Electrochem. Soc.* **147** 4428

[17] Stratford J M, Allan P K, Pecher O, Chater P A and Grey C P 2016 Mechanistic insights into sodium storage in hard carbon anodes using local structure probes *Chem. Commun.* **52** 12430–3

[18] Zhang B, Ghimbeu C M, Laberty C, Vix-Guterl C and Tarascon J M 2016 Correlation between microstructure and Na storage behavior in hard carbon *Adv. Energy Mater.* **6** 1501588

[19] Bommier C, Surta T W, Dolgos M and Ji X 2015 New mechanistic insights on Na-ion storage in nongraphitizable carbon *Nano Lett.* **15** 5888–92

[20] Alvin S, Yoon D, Chandra C, Cahyadi H S, Park J-H, Chang W, Chung K Y and Kim J 2019 Revealing sodium ion storage mechanism in hard carbon *Carbon* **145** 67–81

[21] Li Y, Hu Y-S, Titirici M-M, Chen L and Huang X 2016 Hard carbon microtubes made from renewable cotton as high-performance anode material for sodium-ion batteries *Adv. Energy Mater.* **6** 1600659

[22] Beck F R, Cheng Y Q, Bi Z, Feygenson M, Bridges C A, Moorhead-Rosenberg Z, Manthiram A, Goodenough J B, Paranthaman M P and Manivannan A 2014 Neutron diffraction and electrochemical studies of $Na_{0.79}CoO_2$ and $Na_{0.79}Co_{0.7}Mn_{0.3}O_2$ cathodes for sodium-ion batteries *J. Electrochem. Soc.* **161** A961–7

[23] Viciu L, Bos J W G, Zandbergen H W, Huang Q, Foo M L, Ishiwata S, Ramirez A P, Lee M, Ong N P and Cava R J 2006 Crystal structure and elementary properties of Na_xCoO_2 ($x = 0.32, 0.51, 0.6, 0.75,$ and 0.92) in the three-layer $NaCoO_2$ family *Phys. Rev. B* **73** 174104

[24] Huang Q, Foo M L, Pascal R A, Lynn J W, Toby B H, He T, Zandbergen H W and Cava R J 2004 Coupling between electronic and structural degrees of freedom in the triangular lattice conductor Na_xCoO_2 *Phys. Rev. B* **70** 184110

[25] Willis B T M and Carlile C J 2009 Neutron properties *Experimental Neutron Scattering* (Oxford: Oxford University Press)

[26] Pynn R 1990 Neutron scattering *Neutron Scattering Primer* vol 19 (Los Alamos, NM: Los Alamos Neutron Science Center)

[27] Klosowski P NIST Center for Neutron Research 2019 Neutron Sources (available at: www.ncnr.nist.gov/nsources.html)

[28] Bobrikov I A, Samoylova N Y, Balagurov D A, Ivanshina O Y, Drozhzhin O A and Balagurov A M 2017 Neutron diffraction analysis of structural transformations in lithium-ion batteries *Russ. J. Electrochem.* **53** 178–86

[29] Wang X-L *et al* 2012 Visualizing the chemistry and structure dynamics in lithium-ion batteries by *in-situ* neutron diffraction *Sci. Rep.* **2** 1–7

[30] Peterson V K, Auckett J E and Pang W-K 2017 Real-time powder diffraction studies of energy materials under non-equilibrium conditions *IUCrJ* **4** 540–54

[31] Zhao E *et al* 2020 Neutron-based characterization techniques for lithium-ion battery research *Chin. Phys. B* **29** 018201

[32] Wang H and Wang F 2016 *In situ*, operando measurements of rechargeable batteries *Curr. Opin. Chem. Eng.* **13** 170–8

[33] Shadike Z, Zhao E, Zhou Y-N, Yu X, Yang Y, Hu E, Bak S, Gu L and Yang X-Q 2018 Advanced characterization techniques for sodium-ion battery studies *Adv. Energy Mater.* **8** 1702588

[34] Zhao C, Lu Y, Li Y, Jiang L, Rong X, Hu Y-S, Li H and Chen L 2017 Novel methods for sodium-ion battery materials *Small Methods* **1** 1600063

[35] Shen Q, Liu Y, Jiao L, Qu X and Chen J 2020 Current state-of-the-art characterization techniques for probing the layered oxide cathode materials of sodium-ion batteries *Energy Storage Mater.* **35** 400–30

[36] Squires G L 2012 Introduction *Introduction to the Theory of Thermal Neutron Scattering* 3rd edn (Cambridge: Cambridge University Press)

[37] Goonetilleke D and Sharma N 2019 *In situ* neutron powder diffraction studies *Phys. Sci. Rev.* **4** 1–19

[38] Bee M 1988 *Quasielastic Neutron Scattering: Principles and Applications in Solid State Chemistry, Biology, and Materials Science* (Bristol, England, Philadelphia: Adam Hilger)

[39] Chudley C T and Elliot R J 1960 Neutron scattering from a liquid on a jump diffusion model *Proc. Phys. Soc.* **77** 353–61

[40] Singwi K S and Sjolander A 1960 Diffusive motions in water and cold neutron scattering *Phys. Rev.* **119** 863–71

[41] Hall P L and Ross D K 1981 Incoherent neutron scattering functions for random jump diffusion in bounded and infinite media *Mol. Phys.* **42** 673–82

[42] Berrod Q, Lagrené K, Ollivier J and Zanotti J M 2018 Inelastic and quasi-elastic neutron scattering. Application to soft-matter *EPJ Web Conf.* **188** 1–36

[43] Huang Q, Khaykovich B, Chou F C, Cho J H, Lynn J W and Lee Y S 2004 Structural transition in Na_xCoO_2 with x near 0.75 due to Na rearrangement *Phys. Rev. B* **70** 134115

[44] Medarde M *et al* 2013 1D to 2D Na^+ ion diffusion inherently linked to structural transitions in $Na_{0.7}CoO_2$ *Phys. Rev. Lett.* **110** 266401

[45] Juranyi F *et al* 2015 Dynamics across the structural transitions at elevated temperatures in $Na_{0.7}CoO_2$ *EPJ Web Conf.* **83** 02008

[46] Willis T J, Porter D G, Voneshen D J, Uthayakumar S, Demmel F, Gutmann M J, Roger M, Refson K and Goff J P 2018 Diffusion mechanism in the sodium-ion battery material sodium cobaltate *Sci. Rep.* **8** 1–10

[47] Ma J, Bo S-H, Wu L, Zhu Y, Grey C P and Khalifah P G 2015 Ordered and disordered polymorphs of $Na(Ni_{2/3}Sb_{1/3})O_2$: honeycomb-ordered cathodes for Na-ion batteries *Chem. Mater.* **27** 2387–99

[48] Chen Q, Jalarvo N H and Lai W 2020 Na ion dynamics in P2-$Na_x[Ni_{1/3}Ti_{2/3}]O_2$: a combination of quasi-elastic neutron scattering and first-principles molecular dynamics study *J. Mater. Chem. A* **8** 25290–7

[49] Mendiboure A, Delmas C and Hagenmuller P 1985 Electrochemical intercalation and deintercalation of Na_xMnO_2 bronzes *J. Solid State Chem.* **331** 323–31

[50] Lu Z and Dahn J R 2001 *In situ* x-ray diffraction study of P2-$Na_{2/3}[Ni_{1/3}Mn_{2/3}]O_2$ *J. Electrochem. Soc.* **148** A1225

[51] Kulka A, Marino C, Walczak K, Borca C, Bolli C, Novák P and Villevieille C 2020 Influence of Na/Mn arrangements and P2/P′2 phase ratio on the electrochemical performance of Na_xMnO_2 cathodes for sodium-ion batteries *J. Mater. Chem. A* **8** 6022–33

[52] Rong X *et al* 2019 Anionic redox reaction-induced high-capacity and low-strain cathode with suppressed phase transition *Joule* **3** 503–17

[53] Tapia-Ruiz N, Dose W M, Sharma N, Chen H, Heath J, Somerville J W, Maitra U, Islam M S and Bruce P G 2018 High voltage structural evolution and enhanced Na-ion diffusion in P2-$Na_{2/3}Ni_{1/3-x}Mg_xMn_{2/3}O_2$ ($0 \leqslant x \leqslant 0.2$) cathodes from diffraction, electrochemical and *ab initio* studies *Energy Environ. Sci.* **11** 1470–9

[54] Clément R J, Billaud J, Robert Armstrong A, Singh G, Rojo T, Bruce P G and Grey C P 2016 Structurally stable Mg-doped P2-$Na_{2/3}Mn_{1-y}Mg_yO_2$ sodium-ion battery cathodes with high rate performance: insights from electrochemical, NMR and diffraction studies *Energy Environ. Sci.* **9** 3240–51

[55] Rong X *et al* 2018 Structure-induced reversible anionic redox activity in Na layered oxide cathode *Joule* **2** 125–40

[56] Wang J E, Han W H, Chang K J, Jung Y H and Kim D K 2018 New insight into Na intercalation with Li substitution on alkali site and high performance of O3-type layered cathode material for sodium ion batteries *J. Mater. Chem. A* **6** 22731–40

[57] Li Z-Y, Wang H, Chen D, Sun K, Yang W, Yang J, Liu X and Han S 2018 Improving the performance of layered oxide cathode materials with football-like hierarchical structure for Na-ion batteries by incorporating Mg^{2+} into vacancies in Na-ion layers *ChemSusChem* **11** 1223–31

[58] Han M H, Gonzalo E, Sharma N, López del Amo J M, Armand M, Avdeev M, Saiz Garitaonandia J J and Rojo T 2016 High-performance P2-phase $Na_{2/3}Mn_{0.8}Fe_{0.1}Ti_{0.1}O_2$ cathode material for ambient-temperature sodium-ion batteries *Chem. Mater.* **28** 106–16

[59] Ortiz-Vitoriano N *et al* 2019 High performance P2 sodium layered oxides: an in-depth study into the effect of rationally selected stoichiometry *J. Mater. Chem.* A **7** 21812–26

[60] Xu J *et al* 2014 Identifying the critical role of Li substitution in P2-$Na_x[Li_yNi_zMn_{1-y-z}]O_2$ $(0 < x, y, z < 1)$ intercalation cathode materials for high-energy Na-ion batteries *Chem. Mater.* **26** 1260–9

[61] Kim H, Park I, Seo D-H, Lee S, Kim S-W, Kwon W J, Park Y-U, Kim C S, Jeon S and Kang K 2012 New iron-based mixed-polyanion cathodes for lithium and sodium rechargeable batteries: combined first principles calculations and experimental study *J. Am. Chem. Soc.* **134** 10369–72

[62] Kim H *et al* 2013 Understanding the electrochemical mechanism of the new iron-based mixed-phosphate $Na_4Fe_3(PO_4)_2(P_2O_7)$ in a Na rechargeable battery *Chem. Mater.* **25** 3614–22

[63] Shinde G S *et al* 2020 Revisiting the layered $Na_3Fe_3(PO_4)_4$ phosphate sodium insertion compound: structure, magnetic and electrochemical study *Mater. Res. Express* **7** 014001

[64] Trad K, Carlier D, Croguennec L, Wattiaux A, Ben Amara M and Delmas C 2010 $NaMnFe_2(PO_4)_3$ alluaudite phase: synthesis, structure, and electrochemical properties as positive electrode in lithium and sodium batteries *Chem. Mater.* **22** 5554–62

[65] Liu R *et al* 2020 Recognition of $V^{3+}/V^{4+}/V^{5+}$ multielectron reactions in $Na_3V(PO_4)_2$: a potential high energy density cathode for sodium-ion batteries *Molecules* **25** 1000

[66] Shakoor R A, Seo D-H, Kim H, Park Y-U, Kim J, Kim S-W, Gwon H, Lee S and Kang K 2012 A combined first principles and experimental study on $Na_3V_2(PO_4)_2F_3$ for rechargeable Na batteries *J. Mater. Chem.* **22** 20535–41

[67] Muruganantham R, Chiu Y-T, Yang C-C, Wang C-W and Liu W-R 2017 An efficient evaluation of F-doped polyanion cathode materials with long cycle life for Na-ion batteries applications *Sci. Rep.* **7** 1–9

[68] Kan W H, Huq A and Manthiram A 2015 The first Fe-based Na^+-ion cathode with two distinct types of polyanions: $Fe_3P_5SiO_{19}$ *Chem. Commun.* **51** 10447–50

[69] Titirici M M *et al* 2020 Sodium storage mechanism investigations through structural changes in hard carbons *ACS Appl. Energy Mater.* **3** 9918–27

[70] Bowron D T *et al* 2010 NIMROD: the near and intermediate range order diffractometer of the ISIS second target station *Rev. Sci. Instrum.* **81** 033905

[71] Jian Z, Bommier C, Luo L, Li Z, Wang W, Wang C, Greaney P A and Ji X 2017 Insights on the mechanism of Na-ion storage in soft carbon anode *Chem. Mater.* **29** 2314–20

[72] Li Z, Chen Y, Jian Z, Jiang H, Razink J J, Stickle W F, Neuefeind J C and Ji X 2018 Defective hard carbon anode for Na-ion batteries *Chem. Mater.* **30** 4536–42

[73] Li Z *et al* 2016 High capacity of hard carbon anode in Na-ion batteries unlocked by PO_x Doping *ACS Energy Lett.* **1** 395–401

[74] Li Z *et al* 2017 Mechanism of Na-ion storage in hard carbon anodes revealed by heteroatom doping *Adv. Energy Mater.* **7** 1602894

[75] Wu C-M, Pan P-I, Cheng Y-W, Liu C-P, Chang C-C, Avdeev M and Lin S-K 2017 The mechanism of the sodiation and desodiation in super P carbon electrode for sodium-ion battery *J. Power Sources* **340** 14–21

[76] Wang Y *et al* 2013 A zero-strain layered metal oxide as the negative electrode for long-life sodium-ion batteries *Nat. Commun.* **4** 1–8

[77] Ma X, An K, Bai J and Chen H 2017 $NaAlTi_3O_8$, A novel anode material for sodium ion battery *Sci. Rep.* **7** 1–9

[78] Eguía-Barrio A, Castillo-Martínez E, Zarrabeitia M, Muñoz-Márquez M A, Casas-Cabanas M and Rojo T 2015 Structure of $H_2Ti_3O_7$ and its evolution during sodium insertion as anode for Na ion batteries *Phys. Chem. Chem. Phys.* **17** 6988–94

[79] Kataoka K, Kijima N and Akimoto J 2013 Ion-exchange synthesis, crystal structure, and physical properties of hydrogen titanium oxide $H_2Ti_3O_7$ *Inorg. Chem.* **52** 13861–4

[80] Naeyaert P J P, Avdeev M, Sharma N, Ben Yahia H and Ling C D 2014 Synthetic, structural, and electrochemical study of monoclinic $Na_4Ti_5O_{12}$ as a sodium-ion battery anode material *Chem. Mater.* **26** 7067–72

[81] Woo S H, Park Y, Choi W Y, Choi N-S, Nam S, Park B and Lee K T 2012 Trigonal $Na_4Ti_5O_{12}$ phase as an intercalation host for rechargeable batteries *J. Electrochem. Soc.* **159** A2016–23

[82] Ma Z, Wang Y, Sun C, Alonso J A, Fernández-Díaz M T and Chen L 2014 Experimental visualization of the diffusion pathway of sodium ions in the $Na_3[Ti_2P_2O_{10}F]$ anode for sodium-ion battery *Sci. Rep.* **4** 4–8

[83] Ben Yahia H, Essehli R, Avdeev M, Park J-B, Sun Y-K, Al-Maadeed M A and Belharouak I 2016 Neutron diffraction studies of the Na-ion battery electrode materials $NaCoCr_2(PO_4)_3$, $NaNiCr_2(PO_4)_3$, and $Na_2Ni_2Cr(PO_4)_3$ *J. Solid State Chem.* **238** 103–8

[84] Essehli R, Belharouak I, Ben Yahia H, Maher K, Abouimrane A, Orayech B, Calder S, Zhou X L, Zhou Z and Sun Y-K 2015 Alluaudite $Na_2Co_2Fe(PO_4)_3$ as an electroactive material for sodium ion batteries *Dalt. Trans.* **44** 7881–6

[85] Wang Y, Xiao R, Hu Y S, Avdeev M and Chen L 2015 P2-$Na_{0.6}[Cr_{0.6}Ti_{0.4}]O_2$ cation-disordered electrode for high-rate symmetric rechargeable sodium-ion batteries *Nat. Commun.* **6** 1–9

[86] Wilmer D, Funke K, Witschas M, Banhatti R D, Jansen M, Korus G, Fitter J and Lechner R E 1999 Anion reorientation in an ion conducting plastic crystal—coherent quasielastic neutron scattering from sodium ortho-phosphate *Physica* B **266** 60–68

[87] Gupta M K *et al* 2020 Diffusion of sodium ions in amorphous $Na_2Si_2O_5$: quasielastic neutron scattering and *ab initio* molecular dynamics simulations *Phys. Rev. Mater.* **4** 045802

[88] Jensen A C S, Au H, Gärtner S, Titirici M and Drew A J 2020 Solvation of $NaPF_6$ in diglyme solution for battery electrolytes *Batter. Supercaps* **3** 1306–10

[89] Murphy T, Callear S K, Yepuri N, Shimizu K, Watanabe M, Canongia Lopes J N, Darwish T, Warr G G and Atkin R 2016 Bulk nanostructure of the prototypical 'good' and 'poor' solvate ionic liquids [Li(G4)][TFSI] and [Li(G4)][NO_3] *Phys. Chem. Chem. Phys.* **18** 17224–36

[90] Lucazeau G, Gavarri J R and Dianoux A J 1987 Study of Na^+ motions in βAl_2O_3 by quasi-elastic neutron scattering *J. Phys. Chem. Solids* **48** 57–77

[91] Beevers C A and Ross M A S 1937 The crystal structure of 'beta alumina' $Na_2O·11Al_2O_3$ *Z. Krist. Cryst. Mater.* **97** 59–66

[92] Lucazeau G, Dohy D, Fanjat N and Dianoux A J 1988 Study of the dynamics of a single crystal of Na^+ β-Al_2O_3 by neutron scattering *Solid State Ion.* **28–30** 1611–6

[93] Liu J *et al* 2014 Ionic conduction in cubic $Na_3TiP_3O_9N$, a secondary Na-ion battery cathode with extremely low volume change *Chem. Mater.* **26** 3295–305

[94] Famprikis T, Fauth F, Suard E, Chotard J-N, Islam M S and Masquelier C 2019 A new phase of the Na^+ ion conductor Na_3PS_4 *Prep.* 1–7

[95] Goodenough J B, Hong H Y and Kafalas J A 1976 Fast Na^+ ion transport in skeleton structures *Mater. Res. Bull.* **11** 203–20

[96] Zhang Q, Liang F, Qu T, Yao Y, Ma W, Yang B and Dai Y 2018 Effect on ionic conductivity of $Na_{3+x}Zr_{2-x}M_xSi_2PO_{12}$ ($M =$ Y, La) by doping rare-earth elements *IOP Conf. Ser. Mater. Sci. Eng.* **423** 012122

[97] Jolley A G, Cohn G, Hitz G T and Wachsman E D 2015 Improving the ionic conductivity of NASICON through aliovalent cation substitution of $Na_3Zr_2Si_2PO_{12}$ *Ionics* **21** 3031–8

[98] Logan E R, Tonita E M, Gering K L, Ma L, Bauer M K G, Li J, Beaulieu L Y and Dahn J R 2018 A study of the transport properties of ethylene carbonate-free Li electrolytes *J. Electrochem. Soc.* **165** A705–16

[99] Rudolf P R and Clearfield A 1986 Rietveld refinement results on three nonstoichiometric monoclinic NASICONs *Solid State Ion.* **21** 213–24

[100] Boilot J P, Colomban P and Collin G 1988 Relation structure-fast ion conduction in the NASICON solid solution *Solid State Ion.* **28–30** 403–10

[101] Clearfield A, Subramanian M A, Rudolf P R and Moini A 1986 Stoichiometry, structure and conductivity of NASICON *Solid State Ion.* **19** 13–20

[102] Zhang Z *et al* 2019 Correlated migration invokes higher Na^+-ion conductivity in NaSICON-type solid electrolytes *Adv. Energy Mater.* **9** 1–14

[103] Baur W H, Dygas J R, Whitmore D H and Faber J 1986 Neutron powder diffraction study and ionic conductivity of $Na_2Zr_2SiP_2O_{12}$ and $Na_3Zr_2Si_2PO_{12}$ *Solid State Ion.* **18** 935–43

[104] Deng Y *et al* 2018 Crystal structures, local atomic environments, and ion diffusion mechanisms of scandium-substituted sodium superionic conductor (NASICON) solid electrolytes *Chem. Mater.* **30** 2618–30

[105] Guin M, Dashjav E, Kumar C M N, Tietz F and Guillon O 2017 Investigation of crystal structure and ionic transport in a scandium- based NASICON material by neutron powder diffraction *Solid State Sci.* **67** 30–36

[106] Santhoshkumar B, Rao P L, Ramanathan K V, Bera A K, Yusuf S M, Hathwar V R and Pahari B 2021 Structure and ionic conductivity of $Na_{3+x}Sc_1Si_xP_{3-x}O_{12}$ ($x =$ 0.0, 0.2, 0.4, 0.8) NASICON materials: a combined neutron diffraction, MAS NMR and impedance study *Solid State Sci.* **111** 106470

[107] Lucazeau G, Barj M, Soubeyroux J L, Dianoux A J and Delmas C 1986 Neutron scattering and diffraction study of $Na_3Cr_2P_3O_{12}$, $NaZr_2P_3O_{12}$ and $Na_3ZrMgP_3O_{12}$ *Solid State Ion.* **19** 959–63

[108] Wang H, Chen Y, Hood Z D, Sahu G, Pandian A S, Keum J K, An K and Liang C 2016 An air-stable Na_3SbS_4 superionic conductor prepared by a rapid and economic synthetic procedure *Angew. Chem., Int. Ed.* **55** 8551–5

[109] Zhang Q, Zhang C, Hood Z D, Chi M, Liang C, Jalarvo N H, Yu M and Wang H 2020 Abnormally low activation energy in cubic Na_3SbS_4 superionic conductors *Chem. Mater.* **32** 2264–71

[110] Udovic T J *et al* 2014 Exceptional superionic conductivity in disordered sodium decahydro-closo-decaborate *Adv. Mater.* **26** 7622–6

[111] Tang W S *et al* 2016 Liquid-like ionic conduction in solid lithium and sodium monocarba-closo-decaborates near or at room temperature *Adv. Energy Mater.* **6** 1502237

[112] Tang W S, Dimitrievska M, Stavila V, Zhou W, Wu H, Talin A A and Udovic T J 2017 Order-disorder transitions and superionic conductivity in the sodium nido-Undeca(carba)borates *Chem. Mater.* **29** 10496–509

[113] Dimitrievska M, Shea P, Kweon K E, Bercx M, Varley J B, Tang W S, Skripov A V, Stavila V, Udovic T J and Wood B C 2018 Carbon incorporation and anion dynamics as synergistic drivers for ultrafast diffusion in superionic $LiCB_{11}H_{12}$ and $NaCB_{11}H_{12}$ *Adv. Energy Mater.* **8** 1703422

[114] Tang W S, Unemoto A, Zhou W, Stavila V, Matsuo M, Wu H, Orimo S-I and Udovic T J 2015 Unparalleled lithium and sodium superionic conduction in solid electrolytes with large monovalent cage-like anions *Energy Environ. Sci.* **8** 3637–45

[115] Udovic T J, Matsuo M, Unemoto A, Verdal N, Stavila V, Skripov A V, Rush J J, Takamura H and Orimo S-I 2014 Sodium superionic conduction in $Na_2B_{12}H_{12}$ *Chem. Commun.* **50** 3750–2

[116] Duchêne L, Lunghammer S, Burankova T, Liao W-C, Embs J P, Copéret C, Wilkening H M R, Remhof A, Hagemann H and Battaglia C 2019 Ionic conduction mechanism in the $Na_2(B_{12}H_{12})_{0.5}(B_{10}H_{10})_{0.5}$ closo-borate solid-state electrolyte: interplay of disorder and ion–ion interactions *Chem. Mater.* **31** 3449–60

[117] Chen T-Y *et al* 2018 X-ray absorption spectroscopy and in-operando neutron diffraction studies on local structure fading induced irreversibility in a 18 650 cell with P2-$Na_{2/3}Fe_{1/3}Mn_{2/3}O_2$ cathode in a long cycle test *J. Phys. Chem. C* **122** 12623–32

[118] Liu D *et al* 2019 Review of recent development of *in situ*/operando characterization techniques for lithium battery research *Adv. Mater.* **31** 1–57

[119] Liu J, Didier C, Sale M, Sharma N, Guo Z, Peterson V K and Ling C D 2020 Elucidation of the high-voltage phase in the layered sodium ion battery cathode material P3-$Na_{0.5}Ni_{0.25}Mn_{0.75}O_2$ *J. Mater. Chem. A* **8** 21151–62

[120] Zhu J *et al* 2016 Sodium ion transport mechanisms in antiperovskite electrolytes Na_3OBr and Na_4OI_2: an *in situ* neutron diffraction study *Inorg. Chem.* **55** 5993–8

[121] Liang G, Didier C, Guo Z, Pang W K and Peterson V K 2020 Understanding rechargeable battery function using in operando neutron powder diffraction *Adv. Mater.* **32** 1904528

[122] Vadlamani B, An K, Jagannathan M and Chandran K S R 2014 An *in-situ* electrochemical cell for neutron diffraction studies of phase transitions in small volume electrodes of Li-ion batteries *J. Electrochem. Soc.* **161** A1731–41